

*Ab initio* simulations of liquid semiconductors using the pseudopotential-density functional method

This article has been downloaded from IOPscience. Please scroll down to see the full text article.

2001 J. Phys.: Condens. Matter 13 R817

(<http://iopscience.iop.org/0953-8984/13/41/201>)

View [the table of contents for this issue](#), or go to the [journal homepage](#) for more

Download details:

IP Address: 171.66.16.226

The article was downloaded on 16/05/2010 at 14:56

Please note that [terms and conditions apply](#).

## TOPICAL REVIEW

## ***Ab initio* simulations of liquid semiconductors using the pseudopotential–density functional method**

**J R Chelikowsky<sup>1,3</sup>, Jeffrey J Derby<sup>1</sup>, Vitaliy V Godlevsky<sup>1</sup>,  
Manish Jain<sup>1</sup> and J Y Raty<sup>2</sup>**

<sup>1</sup> Department of Chemical Engineering and Materials Science, University of Minnesota, Minneapolis, MN 55455, USA

<sup>2</sup> Département de Physique, B5, Université de Liège, B4000 Sart-Tilman, Belgium

E-mail: [jrc@msi.umn.edu](mailto:jrc@msi.umn.edu) (J R Chelikowsky)

Received 16 July 2001

Published 28 September 2001

Online at [stacks.iop.org/JPhysCM/13/R817](http://stacks.iop.org/JPhysCM/13/R817)

### **Abstract**

One of the most difficult problems in condensed matter physics is describing the microscopic nature of the liquid state. Owing to the dynamical nature of the liquid state, it is not possible to discuss a particular microscopic structure; only ensemble averages can be specified. Such averages can be performed via well crafted molecular dynamics simulations: the length of the simulation, the size of the ensemble and the nature of the interatomic forces must all be carefully analysed. Historically, a problematic issue in doing such simulations is that of how to describe the interatomic forces in the liquid state. This matter is especially challenging for the melt of semiconductors, such as silicon or gallium arsenide, where the chemical bond contains a strong covalent component. It is difficult to use pairwise interatomic potentials in such cases. Although many-body potentials can be utilized for simulations of these materials, one must map quantum phenomena such as hybridization onto classical interatomic potentials. This mapping is complex and difficult. In this review, we illustrate how one can avoid this problem by utilizing *quantum* forces to simulate liquids. Our focus is on the pseudopotential–density functional method. Within the pseudopotential method, only the valence electrons are explicitly treated and within the density functional theory, exchange and correlation terms are mapped onto an effective one-electron potential. These two approximations allow one to extract quantum forces at every time step of the simulation. The pseudopotential–density functional method is highly accurate and well tested for semiconductors in the solid state, but has only recently been applied to liquids. In this review, we illustrate this approach for a number of semiconducting liquids such as liquid Si, Ge, GaAs, CdTe and GeTe. For these liquids, we will present results for the microstructure, the dynamical properties such as the diffusion constants and the electronic properties such as the conductivity.

<sup>3</sup> Web: <http://jrc.cems.umn.edu/>.

## 1. Introduction

Developing an understanding of the liquid state ( $\ell$ -state) is a formidable challenge, especially for liquid semiconductors. Semiconductors such as Si, Ge and GaAs have been extensively studied in the crystalline phase, but the liquid properties for these semiconductors have not received similar attention. Although  $\ell$ -state Si and Ge are technologically important (e.g. in zone refining in laser-annealed surfaces and crystal growth), the high melting points of semiconductors, such as 1693 K for Si, and the high reactivity of these liquids make experimental examinations difficult [1]. Theoretical studies of liquid semiconductors have also been somewhat limited owing to the complexity of the problem, e.g., large numbers of atoms in motion with little symmetry [2].

One can envision two limiting states of matter: an ideal gas and a perfect crystal. In the ideal-gas limit, the atoms interact rarely and randomly. As a first approximation, the atoms can be treated as point particles undergoing elastic collisions. In the perfect-crystal limit, atoms are associated with a lattice site. They can be described by a fixed periodic array of interacting point particles. Liquids reside between these two limits. The atoms may strongly interact and do so without long-range correlations. They may exhibit local order as for a solid state, but such ordering is temporal and transient fluctuations occur as in a gaseous state. The temporal nature of the  $\ell$ -state can only be described by statistical measures. For example, the microstructure of the liquid can be characterized by a radial distribution or pair correlation function, which gives only an 'average' interatomic distance. Another example concerns the motion of the atoms in the  $\ell$ -state. This motion can be quantified by a diffusion constant that correlates with the root mean square displacement of atoms as a function of time.

Given the nature of the liquid state, it is imperative to construct accurate and representative ensembles [3]. The ensemble must be sufficiently large to capture the essential features of the  $\ell$ -state, but it should not be so large as to preclude an accurate numerical simulation. The ensemble should also contain accurate interatomic interactions at a user-specified temperature and pressure. Replicating the interatomic interactions is the most difficult aspect in the process of simulating an accurate ensemble. Ideally, one would like to treat the interactions in a fully quantum mechanical fashion. In this way, interatomic interactions involving metallic and covalent bonding, hybridization changes or charge transfers would be handled accurately and correctly.

Only recently has it been possible to apply quantum methods to complex systems such as liquids. Early theoretical studies attempted to use empirical, many-body interatomic potentials or semiempirical approximations [4]. More recent methods have focused on quantum calculations [5]. These calculations have become feasible owing both to hardware developments, e.g., parallel computers, and to software developments, e.g., new algorithms. Typically, three approximations are made for *quantum*-based simulations:

- (1) The Born–Oppenheimer approximation. This approximation treats the nuclei as classical particles and allows one to focus on just the electronic degrees of freedom.
- (2) Density functional theory [6]. This theory allows one to map the fully many-electron theory onto a one-particle problem.
- (3) The pseudopotential approximation [7,8]. This approximation reflects the physical content of the Periodic Table. That is, the chemical nature of matter is determined solely by the valence electron configuration.

These approximations are captured within the pseudopotential–density functional method (PDFM) [9]. The PDFM allows one to treat relatively large ensembles of atoms in the liquid

state. It has opened up a new frontier of so-called *ab initio* simulations, i.e., simulations without any *a priori* assumptions about the nature of the interatomic forces.

Several fundamental issues can be addressed with *ab initio* simulations. For example, structural properties of liquids cannot be directly extracted from experimental studies. Only distribution functions or correlation functions can be measured. One cannot obtain ‘snapshots’ of the atomic structure of the melt from experiment. In contrast, theoretical simulations provide a direct window on the microscopic structure of the  $\ell$ -state at any instant of time. Simulations allow one to assess the microstructure, the dynamical and electronic properties and the nature of the bonds in the liquid state. In a heteropolar material such as GaAs, one can establish the probability of like-atom bonds such as an As–As association, which does not occur in the crystalline phase. Moreover, by including an explicit description of the electronic states, it is possible to explore questions about the electronic properties of the liquid such as the conductivity and optical properties of the liquid. Such issues are difficult, if not impossible, to address via classical simulations as these methods do not include a description of the electronic degrees of freedom.

Here we illustrate the PDFM approach to semiconductor liquids. We consider representative examples of group IV (Si and Ge), group III–V (GaAs), group II–VI (CdTe) and group IV–VI (GeTe) semiconductors.

## 2. Preparing a liquid ensemble

In order to describe the behaviour of a liquid, it is necessary to construct an accurate ensemble. Supercells are commonly used to replicate an ensemble for the liquid state [9, 10]. A large unit cell is constructed with periodic boundary conditions. As the simulation evolves, atoms can diffuse seamlessly through the cell. This procedure allows a finite sample to be examined without explicitly considering any surfaces. Of course, introducing such an artificial constraint can alter the dynamics of the system, e.g. it may affect the radial and angular distributions of the liquid state. However, the role of the periodic constraint on physical properties can be tested by increasing the size of the cell and confirming that the structural and dynamical properties are insensitive to the cell size or shape.

To initiate the simulation, atoms are placed within the unit cell either at random or within a crystalline structure. Other than the ease of implementation, a crystalline environment has few advantages over a random one. Local order is preserved in a crystal, as might be expected within the liquid, but a crystalline environment may also lock-in or preserve a configuration not appropriate for the liquid state. The crystalline environment also constrains the shape and size of the supercell. Random configurations do not introduce an initial bias into the liquid state. Of course, the random configurations utilized in simulations are not ‘truly random’, e.g., one does not introduce bond lengths that are unphysically short. For short bond lengths, the interatomic forces can be unrealistically large and produce highly unfavourable energetic configurations. One simple algorithm for generating a random arrangement is to place the first atom randomly in the cell [11]; after this, other atoms are added randomly with one constraint. The constraint is that any added atom resides within a window of possible bond lengths from all other atoms, e.g. any atom–atom distance should not be more than 10% longer (or shorter) than the crystalline bond length. Atoms are added under this constraint until the desired density and stoichiometry are obtained. This procedure avoids biasing the original configuration. It also has the advantage of introducing some higher-energy configurations that allow access to kinetically inhibited configurations.

Once an initial configuration has been obtained, the system is heated to a high temperature to randomize the atomic positions. For example, one might couple the system to a fictive heat

bath and allow the atoms to move a considerable distance from the initial positions. After some time, the system is then cooled, as slowly as is allowed by computational constraints. When the desired temperature is achieved, the system can be removed from the heat bath and statistics obtained from following the equation of motion. A typical thermalizing procedure is illustrated in figure 1.

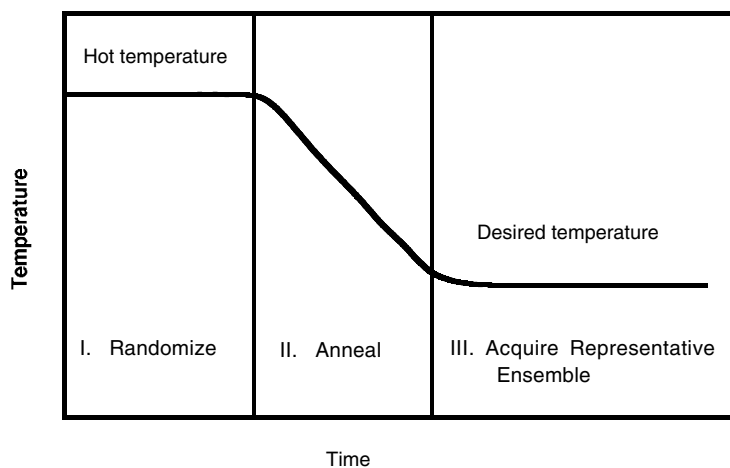


**Figure 1.** A schematic schedule for preparing and simulating a liquid-state ensemble.

The approach to the melting temperature requires some care. For example, one might try to start the system at a low temperature and slowly heat the system to near the melting point. However, since the system is small and contains no defects, the melting process is homogeneous, i.e., it is not initiated by some nucleating defect [12]. For homogeneous melting, the system will not liquefy until raised considerably above the melting point of the crystal, or conversely the liquid state will not solidify until cooled far below the melting point.

Another issue is that of how accurately the melting point of the solid is given by the PDFM. Because of the approximations made in treating the electronic structure problem, one cannot expect to replicate the exact interatomic forces and produce free energies with the observed melting point. Only a few tests of the accuracy of theoretical melting points exist. One of the tests is from Sugino and Car [13]. They examined the melting point of silicon by determining the free-energy differences between the liquid and solid state as calculated via the PDFM. In their simulation, they used multiple reference points [3]; e.g., to determine the free energy of the liquid they referenced the PDFM simulation to a classical simulation of the liquid state, which in turn was referenced to an ideal gas. This procedure, while complex and difficult to implement, found that the simulated melting point was within  $\pm 100$  K of the true melting point. This size of error in the melting point is probably typical, but this issue has not been extensively explored.

The liquid temperature can be controlled by a variety of simulation techniques. These include the use of a Nosé thermostat [14] and the use of Langevin dynamics [15, 16]. There is almost a philosophical issue here as regards the choice of thermostats. Does one consider a small system and suppress dynamical fluctuations away from the desired temperature? Or does one fix an approximate temperature and allow fluctuations to occur as is to be expected for a small system? The former procedure gives better control over the temperature whereas the latter is more physical. Here we focus on Langevin dynamics, which represents the latter

choice. Within Langevin dynamics, the trajectory of each atom is computed from

$$M_i \frac{d\vec{v}_i}{dt} = -M_i \gamma \vec{v}_i + \vec{G}_i(\gamma, T) + \vec{F}_i \quad (1)$$

where  $\vec{F}_i$  is the interatomic force on the  $i$ th particle,  $M_i$  is the mass of the particle and  $\gamma$  is the viscosity of the medium. The particles are subject to rapidly varying random forces,  $\vec{G}_i(\gamma, T)$ . Random forces and viscosity couple the system with the hypothetical heat bath. The dissipative forces are defined by the random Gaussian variables,  $\vec{G}_i$ , such that

$$\langle G_i^\alpha(t) \rangle = 0 \quad (2)$$

$$\langle G_i^\alpha(t) G_j^\alpha(t') \rangle = 2\gamma M_i k_B T \delta_{ij} \delta(t - t'). \quad (3)$$

The angular brackets denote ensemble or time averages and  $\alpha$  stands for the Cartesian component. The interatomic forces,  $\vec{F}_i$ , can be obtained from classical force fields or computed quantum mechanically from the PDFM and the Hellmann–Feynman theorem [17].

In a system with natural or periodic boundary conditions, it can be shown that the canonical distribution is a steady-state solution of the probability distribution associated with the equations of motion, equation (1):

$$P_0 \sim \exp \left[ - \left( \frac{1}{2} \sum_j M_j |\vec{v}_j|^2 + E(\{\vec{R}_j\}) \right) / k_B T \right]. \quad (4)$$

Thus, Langevin dynamics can be used as a rigorous alternative to Nosé dynamics for performing constant-temperature simulations. In contrast to Nosé dynamics, Langevin dynamics includes a physical heat-exchange process that occurs through ‘collisions and friction’ of the particles within the heat bath. The random forces establish the temperature of the system from the fluctuation-dissipation theorem [15]. The energy pumped into the system by the random white noise is dissipated by the viscous forces.

The stochastic nature of the Langevin simulation is highly effective in randomizing the system. As the system is annealed, Langevin dynamics extracts energy from the system until the desired temperature is achieved. Once the system is thermalized, the viscosity term can be zeroed and the system transformed from a canonical to a microcanonical ensemble. Within the microcanonical ensemble one can examine diffusion and other dynamical properties. The chief concern is the size of the ensemble, or the supercell. Provided that the cell is sufficiently large, fluctuations around the desired temperature will be suppressed.

Because of some technical issues, the equations of motion are usually integrated using a Verlet or modified Verlet algorithm [18]. The time steps are taken such that energy is conserved when Newtonian dynamics is utilized. Typically, the error in the energy conservation is at least one to two orders of magnitude less than the fluctuations in the kinetic (or potential) energies during the simulation. The viscosity parameter might be 0.001 au (atomic units  $e = \hbar = m = 1$ ) and the time step might be  $\Delta t = 150$ – $300$  au depending on the atomic mass of the constituent species. Simulation times can vary, but normally a minimum of  $\sim 10^3$  time steps is employed. Since 1 au of time is 0.024 fs, a simulation run in real time usually takes 5–10 ps. Of course, classical simulations for liquids can be much longer than this, e.g.,  $\sim 1$  ns.

### 3. Quantum interatomic forces in the liquid state

Simulations of liquids were primarily performed by utilizing classical potentials before methods were developed for calculating quantum forces. A key step in this evolution was the application and extension of the PDFM to molecular dynamics simulations. Car and Parrinello (CP) were among the first workers to perform *ab initio* molecular dynamics simulations for

liquids and other systems [5]. In the CP method, the nuclear degrees of freedom are treated classically and the electronic degrees of freedom are treated via fictive electronic dynamics.

An alternative way to perform simulations is to treat the electronic degrees of freedom by means of *real* dynamics, i.e., to consider the quantum forces between particles at each time step in the simulation. In this procedure, sometimes known as Born–Oppenheimer molecular dynamics (BOMD) simulation, the system is quenched at every time step to the Born–Oppenheimer surface and the electronic part of the problem solved via a self-consistent field [19]. One might conclude that performing a fully self-consistent calculation at every step would be computationally intensive. However, because the forces are real, one can take significantly larger time steps than within the CP method. The longer time step easily compensates for the extra computational load in obtaining a full self-consistent solution, e.g., often BOMD can have time steps  $\sim 100$  times longer than in CP dynamics. Other advantages of BOMD include ease of implementation and handling metallic systems. This latter is straightforward. At every time step, the electronic levels are occupied as for a static system. One can also utilize level broadening to avoid problems that occur when level crossings occur.

Within the PDFM, one needs to construct an accurate pseudopotential. A wide variety of prescriptions have been devised for transcribing the all-electron potential to a potential that replicates only the properties of the valence electrons [8, 9]. A popular version of *ab initio* pseudopotentials has been proposed by Troullier and Martins [20]. As for other approaches, the ion core pseudopotentials are determined by inverting the Kohn–Sham equations for an atom. The ion core potential is transferable to other configurations as the potential corresponds to the nuclear and ‘inert’ core electrons, both of which are not strongly dependent on the bonding environment. As an example, in silicon the 3s and 3p states would be treated as valence states and the ion core ( $1s^2 2s^2 2p^6$ ) states are taken to be chemically inert. The ion core pseudopotential corresponds to a  $\text{Si}^{4+}$  configuration. Details of the pseudopotential construction can be found elsewhere [9].

Once the pseudopotential has been determined, the resulting eigenvalue problem needs to be solved for the system of interest:

$$\left( \frac{-\hbar^2 \nabla^2}{2m} + V_{ion}^p(\vec{r}) + V_H(\vec{r}) + V_{xc}[\vec{r}, \rho(\vec{r})] \right) \phi_n(\vec{r}) = E_n \phi_n(\vec{r}) \quad (5)$$

where  $V_{ion}^p$  is the ionic pseudopotential for the system. Since the ion cores can be treated as chemically inert and highly localized, it is a simple matter to write

$$V_{ion}^p(\vec{r}) = \sum_{\vec{R}_a} V_{ion,a}^p(\vec{r} - \vec{R}_a) \quad (6)$$

where  $V_{ion,a}^p$  is the ion core pseudopotential associated with the atom,  $a$ , at a position  $\vec{R}_a$ .

A complicating issue in setting up an algorithm is the ionic pseudopotential term. The interactions between valence electrons and pseudo-ionic cores may be separated into a local potential and a Kleinman and Bylander [21] form of a non-local pseudopotential in *real space* [20]:

$$V_{ion}^p(\vec{r}) \psi_n(\vec{r}) = \sum_a V_{loc,ion}(|\vec{r}_a|) \psi_n(\vec{r}) + \sum_{a,n,lm} G_{n,lm}^a u_{lm}(\vec{r}_a) \Delta V_l(r_a) \quad (7)$$

$$K_{n,lm}^a = \frac{1}{\langle \Delta V_{lm}^a \rangle} \int u_{lm}(\vec{r}_a) \Delta V_{l,ion}(r_a) \psi_n(\vec{r}) d^3r \quad (8)$$

and  $\langle \Delta V_{lm}^a \rangle$  is the normalization factor:

$$\langle \Delta V_{lm}^a \rangle = \int u_{lm}(\vec{r}_a) \Delta V_l(r_a) u_{lm}(\vec{r}_a) d^3r \quad (9)$$

where  $\vec{r}_a = \vec{r} - \vec{R}_a$ , and the  $u_{lm}$  are the atomic pseudopotential wave functions of the angular momentum quantum numbers  $(l, m)$  from which the  $l$ -dependent ionic pseudopotential,  $V_l(r)$ , is generated.  $\Delta V_{l,ion}(r) = V_{l,ion}(r) - V_{loc,ion}(r)$  is the difference between the  $l$ -component of the ionic pseudopotential and the local ionic potential. The decomposition into various angular momentum parts is standard practice in pseudopotential theory. By referencing the significant  $l$ -components of the potential to a reference potential, one can avoid projecting out at least one component. For example, in silicon, we might choose the  $l = 0$  component to be local and consider only two non-local components involving p–s differences,  $\Delta V_{l=1,ion} = V(l = 1) - V(l = 0)$ , and d–s differences,  $\Delta V_{l=2,ion} = V(l = 2) - V(l = 0)$ . Implicit in this assumption is that the high-angular-momentum components are not significant and/or they can be approximated by the local potential.

At this point, it is worth summarizing the relevant approximations. We have used density functional theory to map the all-electron problem into a one-electron problem. Commonly the local density approximation is used in this context. We have made the pseudopotential approximation to eliminate the core electrons and allow us to use simple bases to describe the wave functions. Finally, we have used the Born–Oppenheimer approximation to separate the nuclear and electronic degrees of freedom. Of these approximations, the local density approximation is the weakest.

Once the eigenvalue problem is solved, the total energy of the system,  $E_{tot}$ , can be evaluated from [22]:

$$E_{tot} = \sum_{occup} E_n - \frac{1}{2} \int d^3r \rho(\vec{r}) V_H(\vec{r}) + \int d^3r \rho(\vec{r}) (E_{xc}[\vec{r}, \rho(\vec{r})] - V_{xc}[\vec{r}, \rho(\vec{r})]) + E_{i-i}[\vec{R}_a] \quad (10)$$

where  $E_{i-i}$  is the ion–ion repulsion. If one knows the behaviour of the total energy as a function of atomic positions, it is possible to compute interatomic forces and perform *ab initio* molecular dynamics. It should be emphasized that the local density approximation (LDA) applies to the ground state; it is not strictly appropriate to describe excited-state properties using the LDA eigenvalues [6].

Since the pseudopotential is weak, simple basis sets such as a plane-wave basis can be quite effective for crystalline matter. For example, in the case of crystalline silicon only  $\sim 50$  plane waves per atom are required for well converged wave functions and eigenvalues [9]. The resulting matrix representation of the Schrödinger operator is dense in Fourier (plane-wave) space, but it need not be formed explicitly [20, 23]. The plane-wave method uses a basis of the form

$$\psi_{n,\vec{k}}(\vec{r}) = \sum_{\vec{G}} \alpha_n(\vec{k}, \vec{G}) \exp(i(\vec{k} + \vec{G}) \cdot \vec{r}) \quad (11)$$

where  $\vec{k}$  is the wave vector for the  $n$ th band state,  $\vec{G}$  is a reciprocal-lattice vector and  $\alpha_n(\vec{k}, \vec{G})$  represent the coefficients of the basis. For periodic systems,  $\vec{k}$  is a good quantum number and the Bloch form (equation (11)) holds. If supercells are used, one still has a periodic system. However,  $\vec{k}$ , has no physical meaning other than reflecting the artificial periodicity of the system.

A variety of methods have been developed to find the eigenvalue/eigenvector pairs for the secular equations using a plane-wave basis. These methods extract the pairs using iterative solutions, e.g., generalized Davidson methods. Details can be found in the literature [23]. Once the wave functions have been determined, the forces can be determined via the Hellmann–Feynman theorem [24]. For a converged system, the electronic contributions to the interatomic



forces are given by

$$\begin{aligned} \vec{F}_i^{elec} = & -i\Omega_a \sum_{\vec{G}} \vec{G} V_{ion,local}(\vec{G}) \rho(\vec{G}) \exp(i\vec{G} \cdot \vec{r}) \\ & + i\Omega_a \sum_{l,n,\vec{k},\vec{G},\vec{G}'} [(\vec{G}' - \vec{G}) \alpha_n^*(\vec{k}, \vec{G}) \alpha_n(\vec{k}, \vec{G}')] \\ & \times \Delta V_{l,ion}(\vec{k} + \vec{G}, \vec{k} + \vec{G}') \exp(i(\vec{G} - \vec{G}') \cdot \vec{r})]. \end{aligned} \quad (12)$$

The total force is given by this term plus the ion–ion repulsion term, which can be evaluated using Ewald summations [22, 24].

There is a subtle issue involved with the evaluation of the forces or other properties that require summations over the wave vector,  $\vec{k}$ . Bloch's theorem relates the wave functions from one unit cell to those of another by describing how the phase of the wave functions changes from one cell to another (equation (11)). For a supercell, this phase has *no* physical meaning. The periodic boundary conditions do not reflect the properties of the actual liquid state. If any physical properties, such as the diffusion, electronic conductivity or viscosity, strongly depend on the details of the summation over  $\vec{k}$ -states, then the supercell is probably too small to reflect the true properties of the  $\ell$ -state. Provided that the cell is sufficiently large, all the properties of the liquid can be characterized by taking the  $\vec{k} = 0$  state alone. Of course, this is true for a crystal too. If one takes a sufficiently large unit cell, the bands are all 'folded back' to the origin.

The forces from equation (12) can be used in the dynamical description of the liquid, e.g., in the Langevin simulations. They represent the true forces as determined with the PDFM. As such, the simulations that incorporate these quantum forces are often called '*ab initio* simulations'. This is in contrast to simulations that use interatomic force fields fitted to classical interatomic potentials. For example, the very popular interatomic potentials for silicon such as the Stillinger–Weber potentials [4] are fitted to experimental databases and cannot be called first-principles or *ab initio* potentials.

## 4. Properties of liquids from *ab initio* simulations

### 4.1. Microstructure of liquids

A number of properties of liquids can be obtained from *ab initio* simulations. With the possible exception of thermodynamic properties, the microstructure of liquids is the most fundamental materials property. If the structural properties of a system are unknown, it is virtually impossible to predict or understand other properties. Unfortunately, no experimental techniques are available for probing the atomistic structure of the liquid, save in an average sense. Both x-rays and neutron scattering can extract a structure factor,  $S(q)$ , for the liquid state [1]. The structure factor for an elemental liquid can be expressed as

$$S(q) = 1 + \frac{4\pi\rho_0}{q} \int_0^\infty [g(r) - 1] \sin(qr) r \, dr \quad (13)$$

where  $\rho_0$  is the macroscopic density of the liquid and  $g(r)$  is the radial distribution or pair correlation function.

Determining the radial distribution function is complicated by the use of supercells. The value of  $g(r)$  becomes unphysical for large  $r$  owing to the artificial periodicity of the supercell. For example, if one considers a cubic cell of size  $a$ , then for  $r > a$  the positions of the atoms are precisely correlated.

For a compound liquid, the definition of the structure factor is modified. In particular, if one has two species ( $\alpha$ ,  $\beta$ ), the structure factor can be written as

$$S_{\alpha\beta}(q) = \delta_{\alpha\beta} + \frac{4\pi\rho_{\alpha\beta}}{q} \int_0^\infty [g_{\alpha\beta}(r) - 1] \sin(qr) r \, dr \quad (14)$$

where  $\rho_{\alpha\beta}$  is a partial density. Unlike theoretical simulations, experimental probes cannot directly separate the contributions of the partial components. From theoretical work, it is possible to find the density of just the  $\alpha$ -species or the radial distribution of the  $\beta$ -atoms around an  $\alpha$ -atom. If one knows the appropriate scattering parameters, one can compare calculations with neutron or x-ray scattering experiments. For example, the total structure function for a 50–50 alloy of  $\alpha$  and  $\beta$  can be expressed as a linear combination of the partial structure factors,  $S_{\alpha\alpha}(q)$ ,  $S_{\alpha\beta}(q)$  and  $S_{\beta\beta}(q)$ , normalized by the scattering lengths ( $l_\alpha$ ,  $l_\beta$ ) [25]:

$$S(q) = \frac{l_\alpha^2 S_{\alpha\alpha}(q) + 2l_\alpha l_\beta S_{\alpha\beta}(q) + l_\beta^2 S_{\beta\beta}(q)}{l_\alpha^2 + l_\beta^2} \quad (15)$$

to find a value of  $S(q)$ , one needs only the ratio of the scattering lengths:  $l_\alpha/l_\beta$ . The partial structure factors are obtained from partial radial distribution functions via a Fourier transformation. One technical issue centres on how one performs the transformation from  $g(r) \rightarrow S(q)$ . For a supercell geometry, one must truncate the transform for large  $r$  carefully. Often various filtering techniques are used to construct the transformation. These filtering methods constrain  $g(r)$  to unity for large  $r$ . Similar problems exist when one tries to compute the radial distribution from experiment. In going from  $S(q) \rightarrow g(r)$ , the inverse Fourier transform cannot be extended for  $q \rightarrow \infty$ . Moreover, the experiment can often contain noise from poor statistics just as the theory can contain errors from poorly sampling an ensemble owing to short simulation times or a small supercell.

We also note that it is possible to compute higher-order correlation functions, e.g., one can compute angular distributions or three-body correlation functions. Of course, while these functions may be readily computed, there is no simple way to extract such functions with experiment.

#### 4.2. Dynamical properties of liquids: diffusion

Diffusion constants are important parameters for characterizing the liquid and as input into modelling heat and mass flow in crystal growth simulations. However, these physical parameters are difficult to measure. The diffusion constant can be determined from [26]

$$D = \lim_{t \rightarrow \infty} \frac{\langle [R(t)]^2 \rangle}{6t} \quad (16)$$

where

$$\langle [R(t)]^2 \rangle = \frac{1}{N} \sum_{i=1}^N |\vec{R}_i(t) - \vec{R}_i(0)|^2 \quad (17)$$

and where  $\vec{R}_i(t)$  is the position of the  $i$ th atom at time  $t$ . For compound semiconductors, a diffusion constant can be defined for each species, e.g., the diffusion of Cd in liquid CdTe can be obtained by examining the positions of the Cd atoms in the melt as a function of time.

It is also possible to compute the diffusion constant from a knowledge of the velocity autocorrelation function as defined by

$$Z(t) = \frac{\langle \vec{v}(0) \cdot \vec{v}(t) \rangle}{\langle \vec{v}(0) \cdot \vec{v}(0) \rangle} \quad (18)$$

where  $\bar{v}(t)$  is the velocity of an atom averaged over the ensemble. The diffusion constant is given by

$$D = \frac{kT}{M} \int_0^\infty Z(t) dt \quad (19)$$

where  $M$  is the mass of the atom. These two expressions for  $D$  are equivalent; this is a good consistency check on the quality of the simulation [19, 27].

One technical issue of note: the procedure by which the ensemble is prepared does not always guarantee that the centre-of-mass motion of the supercell is zero. Langevin dynamics is stochastic and conservation of momentum is preserved only in an average sense. Once the Langevin phase of the simulation is terminated, and Newtonian dynamics employed, momentum is rigorously conserved. It is a trivial task to zero any residual centre-of-mass motion during the simulation.

#### 4.3. Electronic properties of the liquid

Once we know that the eigenpairs for a given atomic configuration are obtained, we can calculate the optical conductivity. According to the Kubo–Greenwood expression [28] the real part of the conductivity can be expressed as

$$\sigma_r(\omega) = \frac{2\pi e^2}{3m^2\omega\Omega} \sum_{n,m} \sum_{\alpha=x,y,z} |\langle \psi_m | p_\alpha | \psi_n \rangle|^2 \delta(E_n - E_m - \hbar\omega) \quad (20)$$

where  $E_i$  and  $\psi_i$  are eigenvalues and eigenfunctions and  $\Omega$  is the volume of the supercell. The dipole transition elements  $\langle \psi_m | p_\alpha | \psi_n \rangle$  are taken for between the occupied and empty states. The function is sampled over a number of time steps as the simulation proceeds. Typically, the dielectric properties are converged once a dozen or more time steps are sampled. As for the charge density, often only the  $\vec{k} = 0$  point is taken to evaluate the wave functions required in equation (20).

There are a number of problematic issues associated with the Kubo–Greenwood expression. For example, the energy differences used in evaluating the transitions are often taken to be the Kohn–Sham eigenvalues. It is well known in density functional theory that these transition energies do not represent the true optical transitions; the Kohn–Sham gaps tend to be too small, resulting in the so-called ‘band-gap’ problem [29]. Another issue concerns extrinsic contributions to the conductivity. No impurity scattering is included. Despite these limitations, this formalism gives correct trends and often gives semi-quantitative agreement with experiment.

### 5. Elemental semiconductor liquids: silicon and germanium

In figure 2, the calculated pair correlation functions for Si and Ge liquids are illustrated. These pair correlation functions were obtained by averaging over the liquid structure at different times during the microcanonical (zero-viscosity) simulation. In this case, the last few hundred time steps of the simulation were incorporated into a histogram giving the average radial distribution function. For distances greater than the length of the supercell, no new information is collected in calculating the radial distribution function of the liquid. (It is possible to make use of some information in the ‘corners’ of the supercell, but this procedure is complex and does not significantly enhance the accuracy of the pair correlation function.) In these calculations, the edges of the cubic supercells were equal to 10.48 Å and 11.24 Å for Si and Ge, respectively. Some technical details can be found in reference [30].

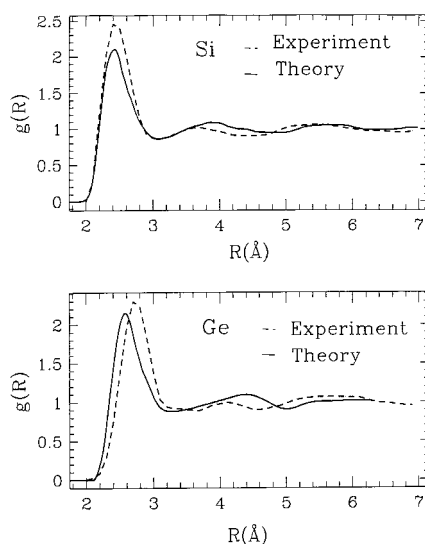


**Figure 2.** Pair correlation function for silicon and germanium liquids. The experiment is from Waseda [31].

One can compare these simulated results with the pair correlation functions extracted from neutron measurements [31]. For silicon, there is a good agreement for the first peak: 2.40 Å from experiment and 2.43 Å from theory. For germanium, the agreement is not as good. A 4% difference exists in the first-peak positions for Ge. This discrepancy may arise from errors in the simulated density. The liquid-state density is often chosen to be that determined by experiment [1]. This value may or may not correspond to the equilibrium density determined by the PDFM. For example, the equilibrium lattice constant predicted from the PDFM can often vary by a few per cent from the measured lattice constant. This difference can result in a 5–10% error in the theoretical density when compared to experiment.

The calculated structure factor function  $S(q)$  is represented in figure 3 along with experimental data [31]. Although we are limited by the size of our supercell in performing the transform of  $g(r)$  into  $S(q)$ , fairly reasonable structure factors can be obtained. In part, this is the case because there is no strong long-range correlation in liquid Si or in liquid Ge. The calculated structure factors for both Si and Ge have an asymmetric shoulder on the first peak, which agrees with the experimental results. The presence of this shoulder indicates that semiconductor liquids have a more complex structure than liquids of simple metals. For example, this shoulder is absent for liquid tin and liquid lead. The shoulder is more pronounced for Si as compared to Ge, consistent with the more metallic behaviour of Ge when compared to Si. Also, the rapid damping of  $g(r)$  shows that the packing of atoms in liquid Si and Ge cannot be replicated by hard-sphere packing as can be done for simple liquid metals.

The origin of this shoulder is related to the depth of the first minimum of  $g(r)$  which follows the first peak. For a liquid with a complex microstructure, the depth of this minimum is accentuated. The position of the first peak in the structure factor has an 8% discrepancy with experimental data for Si and a 10% discrepancy for Ge. The first peak for Ge is shifted to the right more than the corresponding peak in Si.

One can determine the average coordination for the liquid state by integrating the radial distribution function to some cut-off which is usually defined by the first minimum after the first peak in  $g(r)$  [11]. Average coordination numbers of 6.4 for Si and 5.6 for Ge are found.

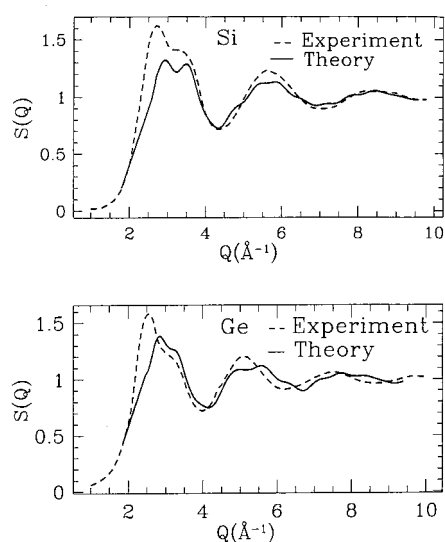


**Figure 3.** Structure factors for silicon and germanium liquids. The experiment is from Waseda [31].

The metallic bonding component of  $l$ -Si or  $l$ -Ge is confirmed by experimental measurements. The liquid state of these semiconductors shows no energy gap. An analysis of the liquid charge density indicates that electrons in the liquid state become delocalized and contribute to the conductivity [32–34]. The experimental results, obtained from the measurements of the Hall coefficient and electrical conductivity, show that the density of conduction electrons increases by  $10^9$ – $10^{11}$  compared to the solid state [1]. While the density of electronic states increases at the Fermi level in the liquid state, the electron scattering rate also increases in the liquid. This latter effect is due to disorder in the liquid state compared to the crystalline state. The combination of these two factors results in an increase of the conductivity by a factor of 20 for  $l$ -Si and by factor of 11 for  $l$ -Ge [1].

In figure 4, we illustrate the root mean square displacement for both  $l$ -Si and  $l$ -Ge. In both cases, the root mean square displacement is quite linear with time, although some small statistical fluctuations are evident. The self-diffusion coefficient for Si is approximately  $1.9 \times 10^{-4} \text{ cm}^2 \text{ s}^{-1}$  from the PDFM. This value is consistent with other *ab initio* calculations using different thermostats or initial conditions, but it is higher than values from simulations based on tight-binding or interatomic potentials. This difference can probably be attributed to the ‘inflexibility’ of a tight-binding basis. A small basis may effectively increase the kinetic barriers owing to the basis having only a few degrees of freedom. The interatomic potentials omit any electronic degrees of freedom and are likely to suffer from the same restrictions. The diffusion coefficient for Ge is  $1.0 \times 10^{-4} \text{ cm}^2 \text{ s}^{-1}$ .

### 6. III–V semiconductor liquids: gallium arsenide

III–V semiconductor crystals differ from Si and Ge semiconductors in that the chemical bond becomes partially ionic and the existence of two species reduces symmetry. In the melt, the changes are more profound; like-atom bonds can be present such as Ga–Ga or As–As.

As in the case of the elemental semiconductors, it is possible to analyse the liquid microstructure. In figure 5, the calculated pair correlation functions are presented. In the upper

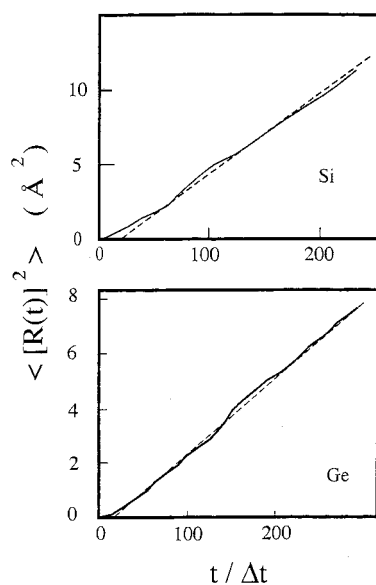


**Figure 4.** The root mean square displacement is plotted versus time. The dashed lines are linear fits to the calculations. The slopes of these lines give the self-diffusion constants for liquid Si and liquid Ge.

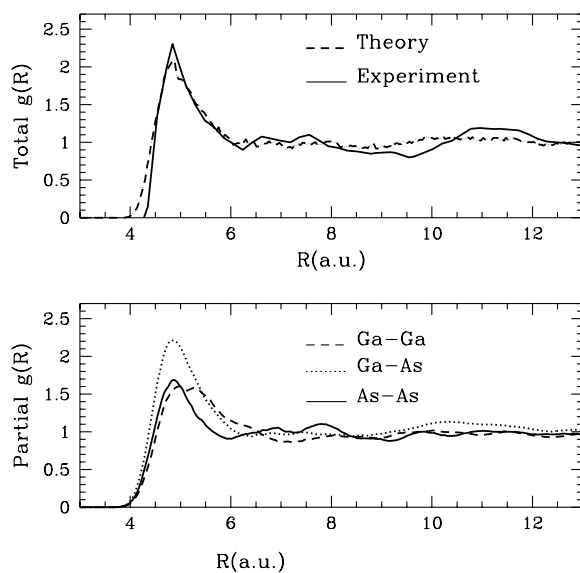


**Figure 5.** Total and partial pair correlation function for liquid GaAs. The experiment is from [35].

part, we display the total radial distribution function from theory compared with the function obtained from  $S(q)$  from experiment [35]. Overall, one finds evidence for weak long-range correlations for  $l$ -GaAs, as for  $l$ -Si and  $l$ -Ge. The second and third peaks are already substantially damped, compared with the first peak. A simple hard-sphere model, or pairwise interatomic interaction model [36], would have considerably stronger long-range correlation.

In these calculations, the  $g(r)$  function has its first minimum at 3.2 Å, which is in good agreement with the experiment. We illustrate the theoretical partial pair correlation functions in the lower part of the figure. It can be seen that there is a certain difference between Ga–Ga and As–As microstructures. The first two peaks in the partial radial distribution functions have different line shapes. In the case of Ga–Ga, there is not a well defined first shell. The peak, corresponding to the first shell, has a wide contour with two shoulders on the right-hand side. The position of the first minimum, which follows the first peak, is noticeably displaced to the right from the first minimum of the As–As radial distribution. In contrast with the Ga–Ga radial distribution, the first peak is well defined in the As–As case. The absence of a well defined first shell suggests a complex structure of the Ga clusters. Peaks and valleys of Ga–Ga and As–As functions are out of phase. This is to be expected for an ionic liquid.

The structure factor,  $S(q)$ , is shown in figure 6. In this figure, we compare the theoretical  $S(q)$  with the experimental result obtained from neutron scattering [35]. In the theoretical  $S(q)$ , the first peak is shifted a little toward higher  $q$ . This shift in the position of the first peak is consistent with previous *ab initio* plane-wave calculations; otherwise the agreement is satisfactory [37]. The structure factor reproduces a shoulder on the first peak. It is instructive to trace how the shoulder is accentuated in liquids of the row IV elements as we move from metallic to covalent liquids [32]. For liquid Pb and Sn the shoulder is absent. It appears first for  $\ell$ -Ge and intensifies for the less metallic  $\ell$ -Si (see figure 3). This shoulder appears to be a signature of local order resulting from covalent-like bonding in the melt.

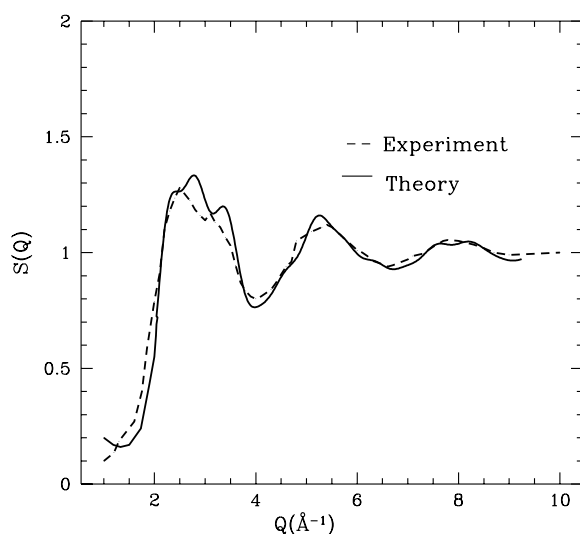


Figure 6. The liquid GaAs structure factor. The experiment is from [35].

Given the total and partial radial distribution functions, it is possible to estimate the coordination numbers as

$$C_{\alpha\beta} = \int_0^{R_{min}} 4\pi r^2 g_{\alpha\beta}(r) dr \quad (21)$$

where  $R_{min}$  is the first-minimum coordinate in  $g(r)$ . We can use the total pair correlation to find  $R_{min}$  (3.2 Å) and extract the partial coordination numbers. To estimate compositional ‘defects’, i.e., like-atom bonds, one can introduce a compositional disorder number (CDN)

defined as the ratio of the numbers of homogeneous and heterogeneous bonds:

$$\text{CDN} = (C_{\alpha\alpha} + C_{\beta\beta})/2C_{\alpha\beta} \quad (22)$$

for the species ( $\alpha, \beta$ ). CDN can be considered an order parameter. For example, in the zincblende structure, CDN is 0, while for a perfect random mix, CDN is 1. CDN can be larger than 1 if a large anion–anion and cation–cation association takes place. In table 1, coordination numbers are summarized using simulations with and without quantum forces. The largest ‘clusterization’ was obtained in the work based on pairwise interatomic forces [36]. The various *ab initio* calculations for  $g(r)$  yield similar values for the total coordination numbers. The ratio of the numbers of homogeneous and heterogeneous bonds ranges from  $\text{CDN} = 0.6$  to  $\text{CDN} = 0.8$  in PDFM work. For systems with a larger values of CDN, atoms are more likely to have neighbours of the same type of species. Typically an atom of Ga has 46% Ga atoms in its first-shell environment and atom of As has 43% As atoms in its first coordination shell.

**Table 1.** Coordination numbers for liquid GaAs as calculated from various theoretical methods.

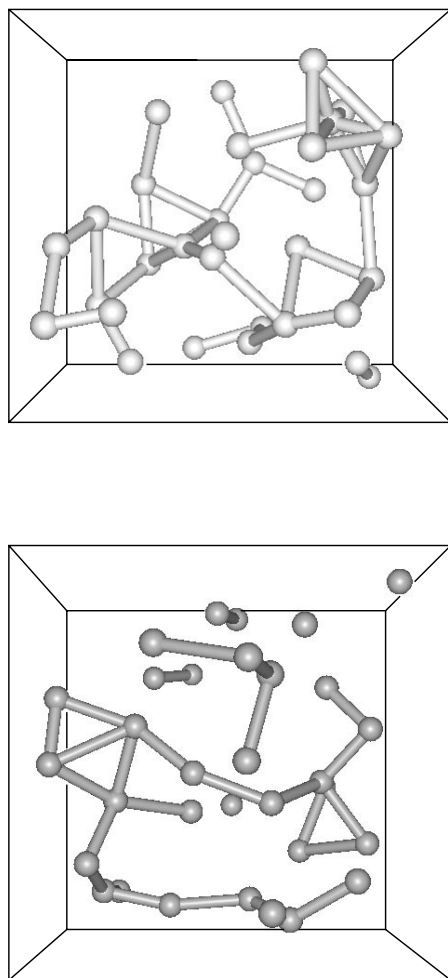
Coordination numbers	$C_{\text{GaAs}}$	$C_{\text{GaGa}}$	$C_{\text{AsAs}}$	$C_{\text{total}}$	CDN
This work	3.5	3.0	2.6	6.3	0.80
Plane-wave calculations [37]	3.9	2.6	2.2	6.3	0.61
Tight-binding calculations [38]	3.9	2.1	2.1	6.0	0.54
Semiempirical pairwise [36] potential simulations	2.6	3.3	2.6	5.5	1.14

In figure 7 we present a snapshot of the atomic positions during the simulation. To obtain insight into the internal cluster structure, it is instructive to examine the Ga and As atoms separately. In figure 7, we provide two pictures, where atoms of each species are drawn separately. We connect atoms if the distance between them is less than  $R_{\text{min}}$ . One can discern that atoms of Ga and As present two types of interpenetrating structure. Atoms of As tend to form ramified chain-like clusters, with occasional triplets attached to the chain. Atoms of Ga, in turn, tend to form more complex structures with a higher coordination number.

To analyse the cluster structure of  $\ell$ -GaAs in more detail, one can use a ‘common-neighbour’ (CN) analysis [39]. A CN analysis can be thought of as a decomposition of the pair distribution function,  $g(r)$ , according to the environment of the pairs. A pair is considered bonded if the distance between two atoms  $R < R_{\text{min}}$ . A set of two indices ( $i, k$ ) specifies the local environment of the pair. The first index,  $i$ , determines the number of neighbours common to both atoms in the pair. The second index,  $k$ , is the number of bonds between these common neighbours. This classification was applied elsewhere [40,41] for analysis of complex ordering phenomena. In figure 8, the CN indexes are shown for typical clusters in  $\ell$ -GaAs. Numbers in columns represent percentages of pairs which contribute in a given cluster. It is seen that Ga atoms tend to form more complex clusters compared to As atoms. The percentage of the triplet (1, 0) pairs is 44% for Ga, compared to 34% for the case of As. The relative difference is more substantial for (2, 0) and (2, 1) clusters. No such clusters were observed during the microcanonical simulation. These results are in agreement with the suggestion that atoms of As form ramified chain-like twofold-to-threefold clusters that envelop more close-packed clusters of Ga atoms.

The concentrations of like-atom bonds do not confirm the significant association of As atoms suggested in one of the first investigations of liquids as performed by Van Vechten [42,43]. The PDFM simulations suggest that Ga clusters possess a higher coordination number than As clusters. Van Vechten’s conjecture about As clusterization was based on the implicit

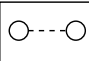
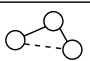
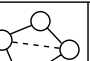
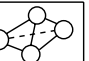




**Figure 7.** A ‘snapshot’ of liquid GaAs. The top figure shows Ga alone; the bottom figure illustrates the As atoms.

measurement of the enthalpy of As clusterization by Arthur [44]. The As aggregation in  $\ell$ -GaAs would decrease the different-type-atom miscibility, lowering the mixing entropy. When Van Vechten took the mixing entropy to be 0, he obtained a better approximation to the melting temperature for GaAs following his model. This validated his hypothesis of As clusterization. A later study [45] collected experimental values of the entropy of melting for a number of III–V semiconductors. According to the data, among the listed compounds, GaAs has the largest entropy change upon melting. This is in agreement with the absence of significant clusterization in our simulations.

Charge-density plots for typical triplets of atoms in  $\ell$ -GaAs are shown in figure 9. The Ga–As bond in the liquid resembles the Ga–As bond in the crystal. The Ga–Ga clusters in the liquid are more metallic-like with some agglomeration of charge in the centre, similar to that observed in elemental Ga, which occurs as orthorhombic crystal. One would expect metallic bonding to favour the compact packed clusters observed in the melt. The more covalent As–As bonds are similar to the bonding in crystal As, where p electrons play a dominant role. In the

				
	(0, 0)	(1, 0)	(2, 0)	(2, 1)
<b>Ga</b>	39	44	12	5
<b>As</b>	64	34	2	0

**Figure 8.** Structural analysis of liquid GaAs via a common-neighbour analysis. The numbers in the columns correspond to the percentages of pairs contributing to a given cluster. See the text.

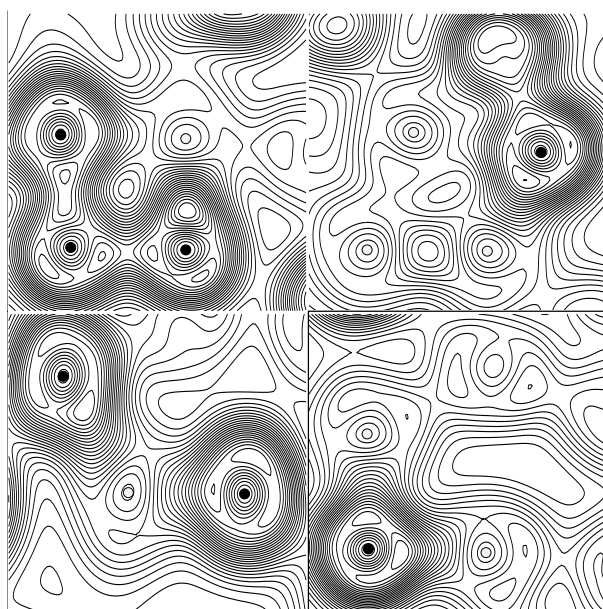


**Figure 9.** Valence 'pseudo-charge'-density plots. Atoms of Ga are open circles; atoms of As are dark dots.

crystal phase, pure As has a rhombohedral lattice. Atoms in this lattice are situated in puckered layers which have hexagonal symmetry. Each atom has three nearest neighbours. In the liquid phase, pure As retains the open threefold structure and the covalent character of the bonds [46]. *l*-As is a semiconductor. Unlike As, metallic *l*-Ga has a compact structure. The coordination number increases from 7, in the *c*-Ga, to  $\sim 9$  in the *l*-Ga [47]. In *l*-GaAs, elemental clusters of Ga and As can be expected to have a tendency to replicate the structural features of pure Ga and pure As liquids, respectively.

We illustrate bond-angular distributions for Ga and As clusters in figure 10. The functions are defined as averages of angles between a reference atom and all pairs of atoms of the same type within a radius  $R_{min}$  of the reference atom. To emphasize the deviation from random distributions, the bond-angle distributions are normalized by  $\sin(\theta)$ . Charge-density plots show a metallic type of bonding for Ga clusters. In the bond-angular distribution a sharp peak occurs at  $60^\circ$ . This peak is associated with Ga clusters and is expected in a close-packed liquid

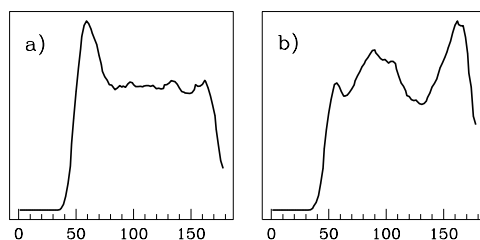


**Figure 10.** Partial angular distribution functions for liquid GaAs in arbitrary units. Ga clusters are given in panel (a), As clusters in panel (b).

or solid. For example, in the hexagonal close-packed structure for a metallic system, we would expect distinctive peaks at  $60^\circ$  and at  $90^\circ$ . Compared to the case for Ga, the covalently bonded clusters of As atoms have a more open structure. The covalent character of As–As bonds defines a strong angle correlation peak near  $90^\circ$ . The peak at  $\sim 160^\circ$  corresponds to an open angle of the chained structures of As. A small shoulder at  $60^\circ$  indicates that a close-packed feature is also present in As clusters. A similar angular distribution can be observed in pure liquid As [46]. The total angular distribution function for  $\ell$ -GaAs (figure 11) is similar to the distribution functions for liquid Si and Ge [30]. Two peaks in the distribution, near  $\sim 60^\circ$  and  $\sim 100^\circ$ , are also present for these liquids. The total angular distribution also agrees well with the other theoretical results obtained with pseudopotentials [37].

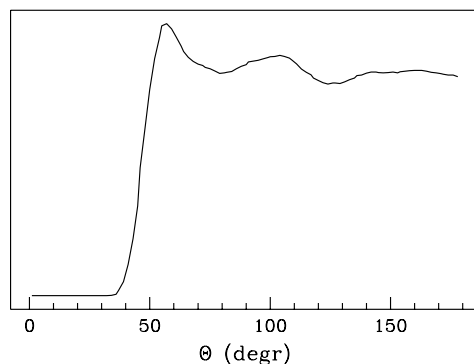


**Figure 11.** The total angular distribution function in arbitrary units for liquid GaAs.

By following the atomic positions in the liquid state as a function of time, we can calculate the diffusion of Ga and As in  $\ell$ -GaAs. In figure 12, the mean square displacement for atoms of Ga and As is displayed. Fitting these curves by a linear time dependence yields  $D_{\text{Ga}} = 1.6 \times 10^{-4} \text{ cm}^2 \text{ s}^{-1}$  and  $D_{\text{As}} = 1.2 \times 10^{-4} \text{ cm}^2 \text{ s}^{-1}$ . These values are in agreement with the previous *ab initio* plane-wave calculations [37]. An average  $D = 1.6 \times 10^{-4} \text{ cm}^2 \text{ s}^{-1}$  is obtained from experimental data [48]. Tight-binding calculations for the diffusion constants [38] yield smaller values:  $D_{\text{Ga}} = 1.0 \times 10^{-4} \text{ cm}^2 \text{ s}^{-1}$  and  $D_{\text{As}} = 0.7 \times 10^{-4} \text{ cm}^2 \text{ s}^{-1}$ . The underestimation of the diffusion constants appears to be a common tendency for a tight-binding model. As in the case of silicon and germanium, we attribute this difference to the ‘inflexibility’ of a tight-binding basis which may effectively increase the kinetic barriers to diffusion.

The electronic density of states (DOS) for  $\ell$ -GaAs is illustrated in figure 13. This DOS was obtained by sampling the  $\Gamma$  point in  $k$ -space and averaging over the ensemble for 200

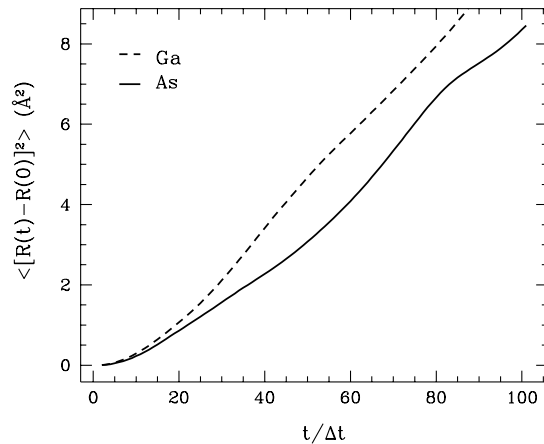


**Figure 12.** The time dependence of the mean square displacement of atoms in liquid GaAs. The simulation temperature is 1550 K.

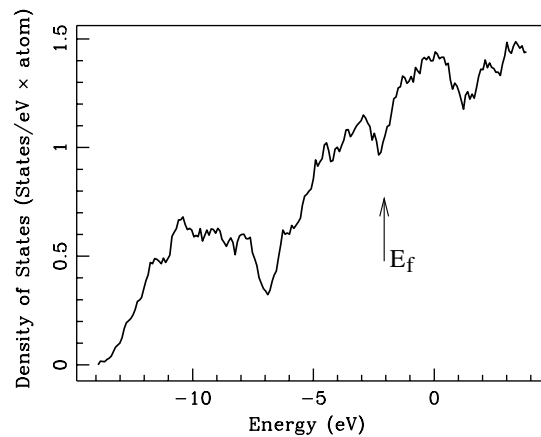


**Figure 13.** The time-averaged density of states for liquid GaAs.

time steps. The DOS is somewhat similar to a free-electron-like function. It is known [1] that the conductivity,  $\sigma$ , changes by a factor of  $\sim 26$  upon melting for GaAs. With a further increase of temperature,  $\sigma$  decreases, demonstrating metallic-like behaviour. This calculated DOS is consistent with the metallic nature of the  $l$ -GaAs.

## 7. II–VI semiconductor liquids: cadmium telluride

Among II–VI semiconductors, CdTe is of special technological interest. Cadmium telluride and its alloys are used to fabricate a wide array of electro-optic devices, high-performance infrared detectors and room temperature radiation detectors. For example, infrared sensors based on epitaxial layers of  $\text{Hg}_{1-x}\text{Cd}_x\text{Te}$  (HgCdTe) are typically grown on single-crystal CdTe substrate. In order to continue the advance of such applications, large, high-quality, single crystals of CdTe are required. However, the growth of such material has proven to be extremely difficult [49–51].

Liquid CdTe ( $\ell$ -CdTe) also presents an interesting subject for fundamental studies [52].  $\ell$ -CdTe exhibits properties which are quite different from those of liquid IV and III–V semiconductors. Neutron scattering experiments [53, 55] suggest that  $\ell$ -CdTe locally conserves its crystalline open-structure environment with the coordination number of  $\sim 4$ . An empirical rule formulated by Joffe and Regel [56] states that a molten or amorphous semiconductor retains its semiconductor properties despite the destruction of long-range order *only if the short-range order of the crystalline phase is preserved*. Indeed, though its electrical conductivity value undergoes a jump by an order of magnitude during melting,  $\ell$ -CdTe remains a semiconductor in the melt: its electrical conductivity *increases* with temperature. This is in contrast to the case for group IV and III–V compounds. These semiconductors become more close packed in the liquid phase with the coordination number increasing to  $\sim 6$  [30, 37, 38, 57] and they undergo a relative volume contraction up to 13% upon melting [1]. It is believed that structural changes occurring in the melting process result in the disruption of covalent bonds and a corresponding metallic delocalization of electrons. This leads to a semiconductor  $\rightarrow$  metal transition [1].

A significant difference in the local order between CdTe and III–V semiconductors is the degree of dissociation of the heteropolar bonds. Following simple thermodynamic estimates, the curvature of the liquidus can be expressed as a function of the entropy change in the solid–liquid transition and the degree of dissociation of anion–cation bonds in the liquid phase [58]. In contrast to those of III–V materials, the phase diagram of CdTe has a sharp hyperbolic liquidus at the congruent point [59]. This liquidus configuration suggests that CdTe has a significant number of heteropolar bonds conserved [60], i.e., in the liquid, the cation tends to exist within a tetrahedral framework of anions, and vice versa. This conservation of local order in  $\ell$ -CdTe serves to verify the Joffe–Regel rule [56]. The assumption that CdTe has more crystalline structural properties preserved in the melt (compared to liquid III–V semiconductors) is reinforced by the small entropy change measured for the solid  $\rightarrow$  liquid phase transition [61]. This is expected if tetrahedral and compositional order in the local environment is more prominent in  $\ell$ -CdTe than a sixfold structure of liquid III–V materials with a higher concentration of stoichiometric defects (or ‘wrong-bond’ defects, which are absent in the crystalline phase of the semiconductor).

Conversely, as we noted for the liquid III–V compounds, the local environment is significantly altered. In addition to the increase of the coordination number, the stoichiometry of the bonds is changed. For instance, for  $\ell$ -GaAs, the dissipation of heteropolar bonds is substantial [60]. The first coordination shell consists of  $\sim 50\%$  of atoms of the same species as the reference atom [11].

The semiconductor behaviour of  $\ell$ -CdTe is observed only in a narrow temperature range immediately above the melting temperature. Upon further heating, at a temperature  $\sim 120$  K higher than the melting point, the electrical conductivity of  $\ell$ -CdTe undergoes a sharp increase and the liquid phase becomes metallic [1]. Gaspard *et al* [55] suggested that  $\ell$ -CdTe undergoes a fourfold  $\rightarrow$  sixfold transformation at higher temperature. This would explain the metallic behaviour of the melt. Also, Glazov *et al* [1] made the hypothesis that atomic chains of Te are an essential feature of  $\ell$ -CdTe. If such chains exist in the liquid, they could be a partial explanation for the difficulty in growing a pure single crystal from a liquid phase. However, this issue has not been clearly resolved. It has also been suggested that if the structure of the melt is close to that of the solid, many nucleation sites may exist, resulting in a number of grain boundaries forming instead of a well defined single crystal.

II–VI semiconductors containing group IIB elements can present severe computational challenges in computations for their electronic structure. Pseudopotentials have great advantages over all-electron methods, as one only needs to solve for the valence electrons. However, for IIB elements such as Cd, it is not clear whether the outer, filled d orbitals can

be treated as part of the ion core. Often, these orbitals possess significant overlap with the *s* valence orbitals and cannot be neglected, especially in describing the structural properties of II–VI semiconductors. On the other hand, treating *d* orbitals as part of the valence shell dramatically increases the complexity of the problem. For example, the number of valence electrons increases from 8 to 18 per cation–anion pair and more than doubles the number of eigenvalues required. Also, the pseudopotential constructed using the filled *d* shell as part of the valence shell is much stronger and more localized than the pseudopotential that is constructed with the *d* orbitals as part of the core. Consequently, more plane waves, or other basis functions, are required for equivalently converged eigenvalues if the outer *d* orbitals are treated explicitly by the pseudopotential.

This matter can be addressed via a *partial-core* pseudopotential [62]. The partial-core pseudopotential treats the *d* orbitals as core states, but each time the exchange–correlation term is calculated for a self-consistent-field calculation, a fixed *d* core charge density is added to the valence charge density. A Cd pseudopotential with the 4*d* electrons omitted altogether results in a substantially underestimated lattice constant and overestimated bulk modulus (see table 2). In contrast, a partial-core pseudopotential for Cd in the CdTe crystal yields a lattice constant within 1% accuracy compared to the experimental value and a bulk modulus within 2% accuracy. Moreover, the CdTe band structure calculated with a pseudopotential that includes the 4*d* orbitals explicitly and the band structure calculated with a partial core for the 4*d* orbitals are nearly identical. In particular, the agreement between the two band structures is excellent for *p* electrons at the top of the valence band and for the conductivity band (figure 14). This is important, because one needs accurate bands near the optical gap to evaluate dipole transitions and calculate the dielectric properties of the crystal. The largest difference is that the partial-core treatment shifts the Te *s* band (the lowest valence band in CdTe) by 1.5 eV. The Te *s* band is a ‘semi-core’ band as it resides about 10 eV below the top of the valence band. As such, its precise placement is not crucial in determining the band configuration near the gap.

**Table 2.** Lattice constants and bulk moduli for the zinc-blende phase of CdTe calculated with different Cd potentials. The cut-off radii used to generate Cd potentials are also presented.

Test	<i>a</i> (Å)	<i>B</i> (GPa)	<i>r<sub>c</sub></i> (for <i>s/p/d</i> in Å)
Cd <sup>2+</sup> 5 <i>s</i> <sup>2</sup> 5 <i>p</i> <sup>0</sup> 5 <i>d</i> <sup>0</sup>	6.13	51	1.38/1.38/1.90
Cd <sup>2+</sup> 5 <i>s</i> <sup>2</sup> 5 <i>p</i> <sup>0</sup> 5 <i>d</i> <sup>0</sup> partial-core correction	6.43	43	1.38/1.38/1.90
Cd <sup>12+</sup> 4 <i>d</i> <sup>10</sup> 5 <i>s</i> <sup>2</sup> 5 <i>p</i> <sup>0</sup>	6.45	47	1.38/1.27/1.69
Experiment [63, 64]	6.48	42	44

It is more convincing to compare the dynamical properties of the liquid with the 4*d* orbitals treated explicitly and implicitly via the partial-core pseudopotential. A molecular dynamics simulation has been performed for an eight-atom supercell for 3 ps. No significant difference between the diffusion constants was observed with the 4*d* orbitals treated explicitly or implicitly in this small test system. We view these comparisons as validating the partial-core correction for elements such as Cd and Zn. However, it should be noted that a similar calculation for Hg is likely to be problematic. In the case of HgX (*X* = group VI element), the Hg 5*d* states strongly overlap the valence band. It is likely that a simulation for HgTe or HgSe will require a pseudopotential with the 5*d* orbitals treated as part of the valence cell.

It is relatively easy to explore a number of different temperature regimes with simulations. Here we consider three general temperature regimes for *ℓ*-CdTe: 800 K, 1370 K (the known

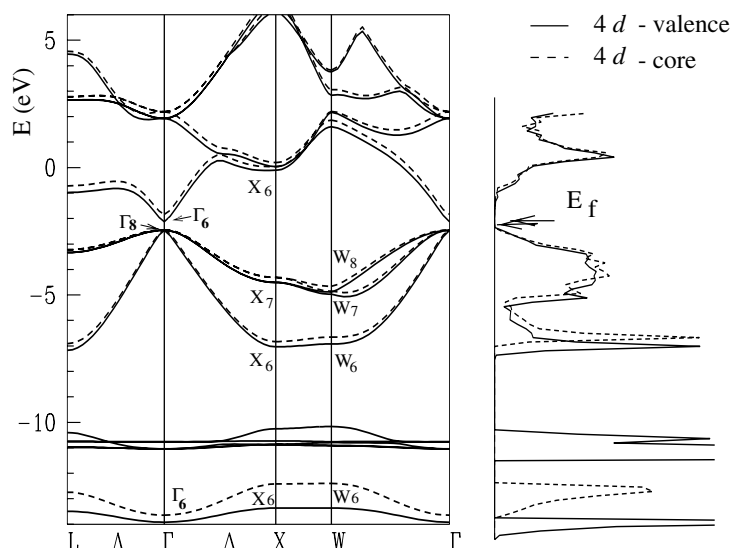


**Figure 14.** The band structure (left panel) and density of states (right panel) for CdTe. Two calculations are shown. The solid lines show results where the 4d electrons are treated as valence electrons. The dashed lines show results where the 4d electrons are included in the core using a partial-core correction scheme (see the text).

melting point) and 3000 K. By examining the self-diffusion of (Cd, Te) in the melt we can verify that these regimes all correspond to liquid-like states. For discussion purposes, we will characterize the 800 K simulation as corresponding to a ‘supercooled state’, the 1370 K simulation as corresponding to the ‘liquid state’ and the 3000 K simulation as corresponding to a ‘superheated state’ of the liquid.

In the crystalline phase, the Cd–Te bond has strong ionic nature, its Phillips ionicity [65] being 0.72. In general, the ionic nature of the material is preserved in the liquid phase. A ‘snapshot’ of the liquid microstructure (figure 15) is taken at one of the time steps during the 3 ps simulation of *l*-CdTe at 1370 K. The charge density is characterized by considering a isocharge surface. This surface is defined by a charge density corresponding to one half of its maximum value. The electronic charge-density isosurfaces appear to be somewhat insensitive to temperature; at least, they appear very similar to the ones presented here. The charge density associated with the Te bonds exhibits pronounced p-electron character, e.g., little amplitude at the origin. Conversely, charge-density configurations associated with the Cd cations tend to be s-like and localized on the atomic sites.

Using the atomic positions at each time step, and averaging the positions over the representative ensemble, one can obtain total pair correlation functions,  $g(R)$ . For supercooled CdTe, we average  $g(R)$  over the last 100 time steps, after the system has become viscous. One can assess the viscosity by examining the diffusion coefficients. For *l*-CdTe and superheated CdTe, we average  $g(R)$  for the last 300 time steps (2.2 ps) of the simulations at 1370 K and 3000 K, respectively. Total pair correlation functions are shown in figure 16.

For all three temperatures, the first peak occurs at 2.8 Å. The first shell can be defined in terms of the coordinate of the first minimum,  $R_{min}$ . As one would expect, as the temperature increases this peak becomes wider (indicating more disorder in the melt) and its amplitude decreases. This results in the shifting of  $R_{min}$  from  $R_{min} = 3.5$  Å (for supercooled Te) to  $R_{min} = 3.6$  Å and 4 Å for *l*-CdTe and superheated CdTe respectively. While supercooled

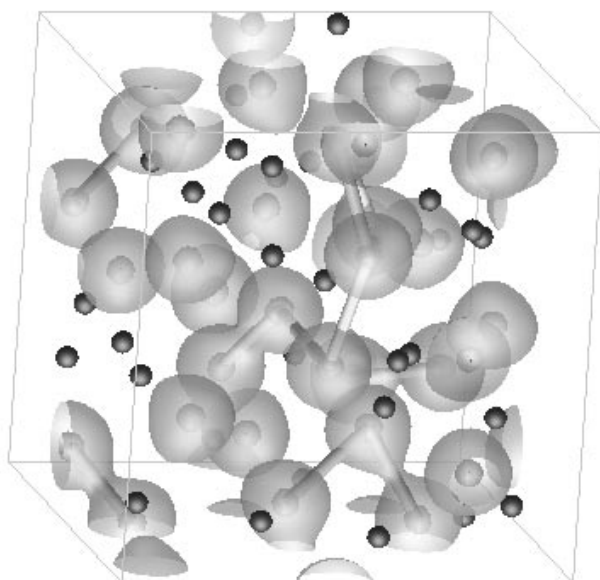


**Figure 15.** A snapshot showing a typical  $\ell$ -CdTe structure in the supercell (see the text). Atoms of Cd are represented by dark spheres; atoms of Te are shown by light spheres.

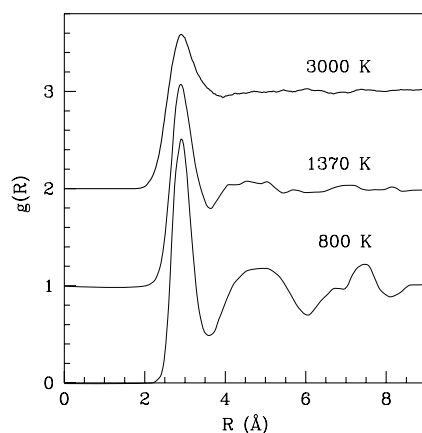


**Figure 16.** Total pair correlation functions for liquid CdTe at different temperatures.

CdTe has well defined first, second and third shells and  $\ell$ -CdTe has well defined first and second shells, the radial distribution function for superheated CdTe becomes 'flat' immediately after the first peak. We find in all cases that the absence of long-range correlation at the distance  $a$  (the length of the supercell  $a = 13.37$  Å) validates *a posteriori* the usage of the 64-atom supercell.

To compare these calculations with neutron scattering experiment results, we can obtain the total structure function as a linear combination of the partial structure factors,  $S_{\text{CdCd}}(q)$ ,  $S_{\text{CdTe}}(q)$  and  $S_{\text{TeTe}}(q)$ , normalized by the scattering lengths (equation (15)). The ratio of the scattering lengths [25] is usually taken to be  $\alpha_{\text{Cd}}/\alpha_{\text{Te}} = 5.8/7.5$ . Partial structure factors are obtained from partial radial distribution functions by a Fourier transformation (equation (14)).



In figure 17, we show the theoretical total structure factors from a PDFM simulation compared with available experiment [53] and the theoretical results obtained from a molecular dynamics simulation based on a Stillinger–Weber-type classical potential [54]. For  $\ell$ -CdTe, the agreement between theory and experiment is good for the third and fourth peaks at  $\sim 5 \text{ \AA}^{-1}$  and  $\sim 7.5 \text{ \AA}^{-1}$  respectively. The agreement between a quantum simulation and Stillinger–Weber-type simulation is excellent for these two peaks. This suggests that short-ranged forces are correctly reproduced by the Stillinger–Weber potential. The PDFM calculations reproduce the structure of the experimental  $1.7 \text{ \AA}^{-1}$  and  $3.0 \text{ \AA}^{-1}$  peaks reasonably well. As the temperature increases and disorder is introduced, features corresponding to long-range correlations (the leading peaks of  $S(q)$ ) become less prominent. As the temperature varies, the second peak also experiences a significant morphological change. At the melting point,  $\ell$ -CdTe has a symmetric form of the peak at  $2.7 \text{ \AA}^{-1}$ . At 3000 K, the peak becomes asymmetric with a pronounced right shoulder. This shoulder is a typical structure for liquid IV and III–V semiconductors which are metallic in the melt (see figure 3).

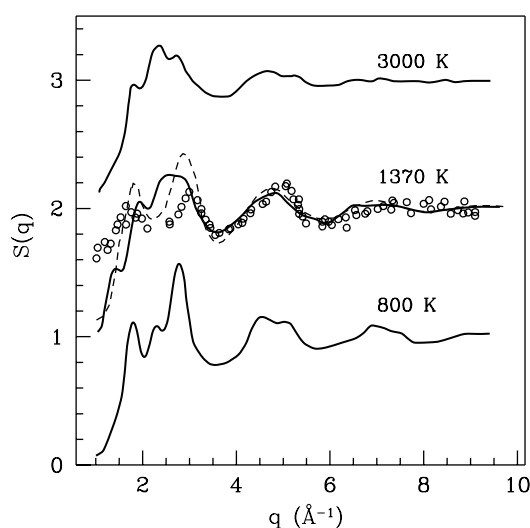


**Figure 17.** Total structure factors. For  $\ell$ -CdTe at the melting temperature we compare our data with available experimental data [53] (dots) and the result obtained with Stillinger–Weber potential simulations [54] (dashed line).

We note that at 3000 K, CdTe is clearly superheated and is metallic. For this temperature, the first peak, at  $1.9 \text{ \AA}^{-1}$ , almost merges with the second peak. This is very different from the situation for supercooled CdTe, where the first and the second peaks become more pronounced and separated. The first peak moves to lower  $q$ , at  $1.8 \text{ \AA}^{-1}$ , while the second peak becomes asymmetric with a noticeable left shoulder.

We estimate the total and partial coordination numbers from the corresponding pair correlation functions from equation (21). The values of  $R_{min}$  vary somewhat with temperature. Typical values are  $R_{min} = 3.5 \text{ \AA}$ ,  $3.6 \text{ \AA}$  and  $4.0 \text{ \AA}$  for the supercooled, liquid and superheated phases respectively. To estimate quantitatively the concentration of the stoichiometry defects in the system, one can introduce a compositional disorder number as in equation (22). In table 3, we present coordination numbers and CDNs at three different temperatures. While the qualitative trends are clear, the CDNs are somewhat sensitive to the choice of  $R_{min}$ . For  $\ell$ -CdTe, the average number of neighbours in the first shell is 4.4, indicating that CdTe retains

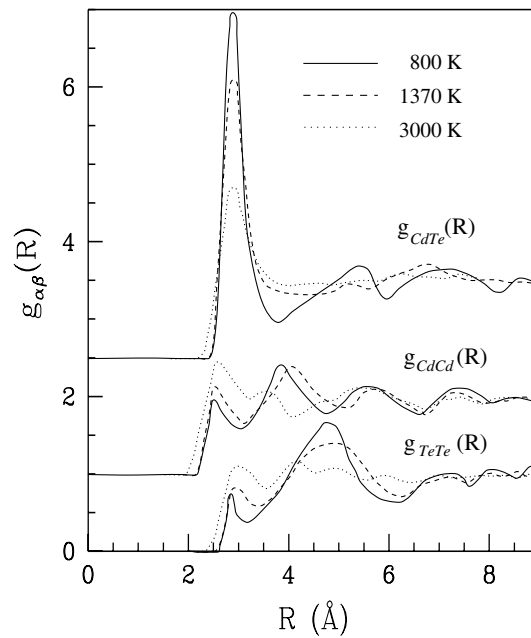
**Table 3.** Total and partial coordination numbers for CdTe at three different temperatures.

	$C_{tot}$	$C_{CdTe}$	$C_{CdCd}$	$C_{TeTe}$	CDN
800 K	4.2	3.2	1.4	0.6	0.3
1370 K	4.4	3.3	1.5	0.9	0.4
3000 K	6.5	3.7	3.2	2.5	0.8

its open structure upon melting. This is different from the situations for the more close-packed liquid IV and III–V semiconductors where the coordination number is  $\sim 6$ .

Upon further heating, CdTe transforms into a more close-packed phase with  $C_{tot} = 6.5$ . The CDN of  $\ell$ -CdTe is 0.4. This is in agreement with the assumption [60] that the degree of dissociation of heterogeneous bonds in  $\ell$ -CdTe is noticeably smaller than in III–V melts. The structure of these melts is close to a random mix with  $CDN \sim 1$  [59]. At sufficiently high temperatures, one expects no local order. For the case of superheated CdTe,  $CDN = 0.8$ , approaching the random-mix limit of  $CDN = 1$ .

Partial pair correlation functions are presented in figure 18. For  $\ell$ -CdTe and supercooled CdTe, the correlation of the reference atom with the second shell is stronger than with the first one in both  $g_{CdCd}$  and  $g_{TeTe}$  radial distributions. For superheated CdTe the first and second shells are comparable in weight. Clusters of Cd and Te retain some long-range structure, as the noticeable correlation in the third and even the fourth peaks indicates. The positions of the first two Te–Te shells are at  $\sim 2.9$  Å and  $\sim 4.8$  Å. This is opposite to the case of the compact shells in Cd clusters with the positions at  $\sim 2.6$  Å and  $\sim 4.0$  Å.


**Figure 18.** Partial radial distribution functions,  $g_{CdTe}$ ,  $g_{CdCd}$  and  $g_{TeTe}$  (see the text).

In simulations for  $\ell$ -CdTe, atoms of Te have been observed to form branched chains. It is known that the trigonal phase of crystalline Te consists of close-packed infinite and parallel helicoidal chains. Both experimental [66] and theoretical [67] studies suggest that Te forms

chain-like structures in the elemental liquid phase. In general, it appears that short-ranged configurations in the melt often replicate structural characteristics of the elemental constituents. In liquid CdTe, the elemental characteristic appears to be chains of Te.

One can follow the behaviour of the Te clusters as the temperature increases from 800 K to 3000 K. In simulated supercooled CdTe, the Te chains are short with the maximum length of 3–4 links. Only  $\sim 30\%$  of Te atoms are bonded in these formations. As the temperature increases, the length of the chains increases. Te helicons become more irregular and ‘twisted’; the chains start to ramify. At the melting temperature, there are Te filaments reaching the length of the supercell. Because of the imposed periodicity of the system, some of the Te chains terminating at the opposite sides of the supercell become ‘infinite’. We find no Te triplets or tetrahedra in the liquid. At 1370 K, 45% of Te atoms are bound with each other. As the temperatures grows further, the chains transform into more complex clusters with a higher coordination number  $C_{\text{TeTe}} = 2.5$ .

In figure 19 configurations of Te clusters are illustrated at different temperatures. To simplify the appearance of the plot, only atoms of Te are shown. Atoms are considered to be bonded if the distance between them is less than the first-minimum distance,  $R_{\text{min}}$ , of the total pair correlation function. The size of the cubic cell shown corresponds to  $2 \times 2 \times 2$  supercell geometry. At 1370 K, infinite helicon chains can be seen in the figure.

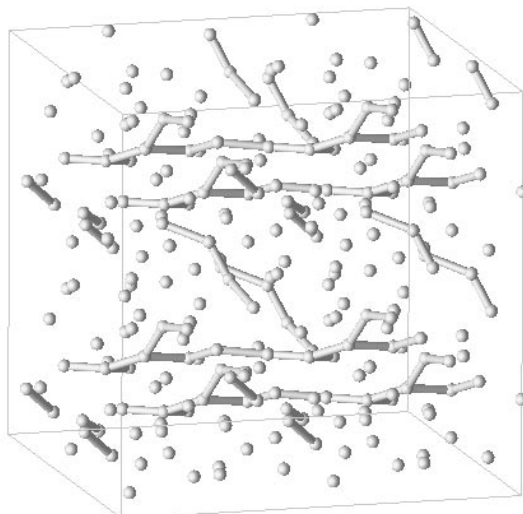


**Figure 19.** Structure of liquid CdTe at various temperatures. The box corresponds to  $2 \times 2 \times 2$  supercell geometry. Only atoms of Te and bonds between them are shown.

Clusters of Cd have a structure different from the structure of Te chains in supercooled CdTe and *l*-CdTe. The difference corresponds to the fact that, for 800 K and 1370 K systems, the coordination numbers  $C_{\text{CdCd}}$  are larger (roughly by a factor of two) than the numbers  $C_{\text{TeTe}}$ . This implies a more close-packed structure for Cd–Cd configurations. Cd ‘clusters’ occur that are composed of tetrahedra, triplets and more complex rings in supercooled CdTe and *l*-CdTe. From the partial angular distribution of the bonds (figure 20), it can be seen that clusters of Cd and Te are drastically different for the 800 K system. The difference diminishes as the temperature increases. In the superheated state, it almost vanishes. The angle,  $\theta$ , corresponding to the open angle in the Te chains, dominates in the Te angular distribution. We find typically  $\theta \sim 160^\circ$ . At variance with the Te clusters, clusters of Cd have the angle

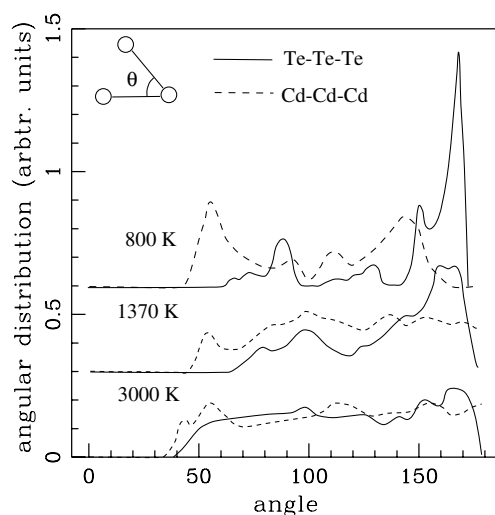


**Figure 20.** Angular distributions of bond angles in Te and Cd clusters. The distributions are normalized by  $\sin(\theta)$ .

$\theta \sim 60^\circ$  prevailing for supercooled CdTe. This angle represents the high concentration of triplets and close-packed Cd clusters. The total angular distribution is shown in figure 21. For superheated CdTe the  $\sim 60^\circ$  angle dominates. As the temperature decreases, the tetrahedral angle starts to dominate.

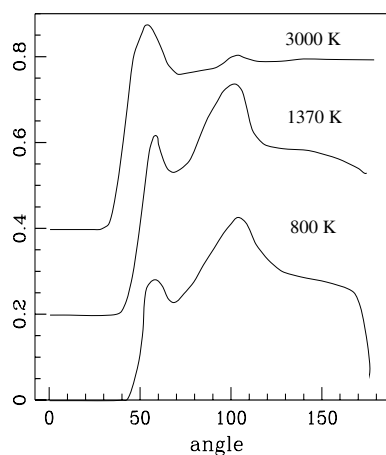


**Figure 21.** Total angular distributions (in arbitrary units) of bond angles. The distributions are normalized by  $\sin(\theta)$ .

Once we know the energy states and wave functions for a given atomic configuration, we can calculate the optical conductivity from equation (20). The real part of the optical conductivity of CdTe at different temperatures is displayed in figure 22. Each curve is the result of averaging several configurations chosen at random from the representative ensembles at each temperature. Typically, only 5–10 configurations are required to obtain a reasonably well converged conductivity. The d.c. conductivity value (at  $\omega = 0$ ) is linearly

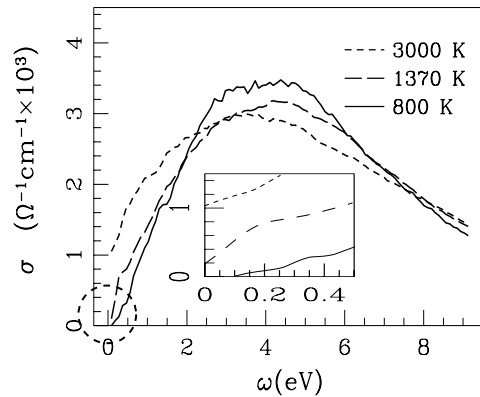


**Figure 22.** The real part of the optical conductivity for liquid CdTe at various temperatures. The circled area is enlarged and shown in the inset.

extrapolated from  $\omega \rightarrow 0$ . As expected for a semiconductor, the d.c. conductivity is vanishingly small for supercooled CdTe. When CdTe melts, the electronic properties undergo a semiconductor  $\rightarrow$  semiconductor-type transition. Specifically, the electric conductivity of the melt increases by a factor of 40, whereas the liquid remains a semiconductor as the d.c. conductivity increases upon further heating [1]. At  $\sim 120$  degrees above the melting point, the conductivity appears to increase more rapidly [1]. The conventional interpretation is that at high temperature, CdTe undergoes a semiconductor  $\rightarrow$  metal transition. However, we note that measuring the conductivity at, or above, the melting point is hindered by the high temperature and the jump-like increase of the conductivity. It is not surprising that experimental values for d.c. conductivity vary by almost a factor of three in the literature [1, 59, 68] from 40 to  $110 \Omega^{-1} \text{cm}^{-1}$ . The d.c. conductivity value obtained within the PDFM simulation is  $\sim 100 \Omega^{-1} \text{cm}^{-1}$  at the melting temperature. This value is in surprisingly good agreement with the experimental results—in particular, given the use of Kohn–Sham eigenvalues, one does not expect an accurate representation of the excitation spectra [29, 69]

As a function of frequency,  $\ell$ -CdTe has a semiconductor-type conductivity: the real part of the conductivity does not have a metallic Drude-like dependence,  $\sigma(\omega) \sim \sigma_0/(1 + \omega^2\tau^2)$ , found for liquid IV and III–V semiconductors [34, 37]. The frequency-dependent conductivity for CdTe peaks at approximately 4 eV and then goes asymptotically to zero as  $1/\omega^2$ .

Temperature significantly alters the behaviour of  $\sigma(\omega)$  at small  $\omega$ . This behaviour can be understood by examining states near the Fermi level. The total and partial density-of-states functions are displayed in figure 23. These curves are the results of averaging over ten atomic configurations taken at random from the corresponding ensemble at each temperature. To obtain the partial DOS functions, a Wigner–Seitz radius corresponding to one half of the cell volume was used to deconvolve the wave function over spherical harmonics around each atom. Each DOS is convoluted with a 0.2 eV Gaussian (full width at half-maximum). To preserve the sharp features of the DOS at the Fermi level, states near the Fermi level ( $E_f \pm 0.5$  eV) are convoluted with 0.05 eV Gaussians. The transition between 0.2 eV and 0.05 eV Gaussians is performed gradually over the energy intervals  $E_f - 1.0 \text{ eV} < E < E_f - 0.5 \text{ eV}$  and  $E_f + 0.5 \text{ eV} < E < E_f + 1.0 \text{ eV}$ .

At 800 K, there is a ‘dip’ at the Fermi level. Since the DOS is an average over a number of atomic configurations, where the Fermi energy takes slightly different values, a well defined gap is not apparent in the DOS curve. In particular, at each time step a small band gap can exist

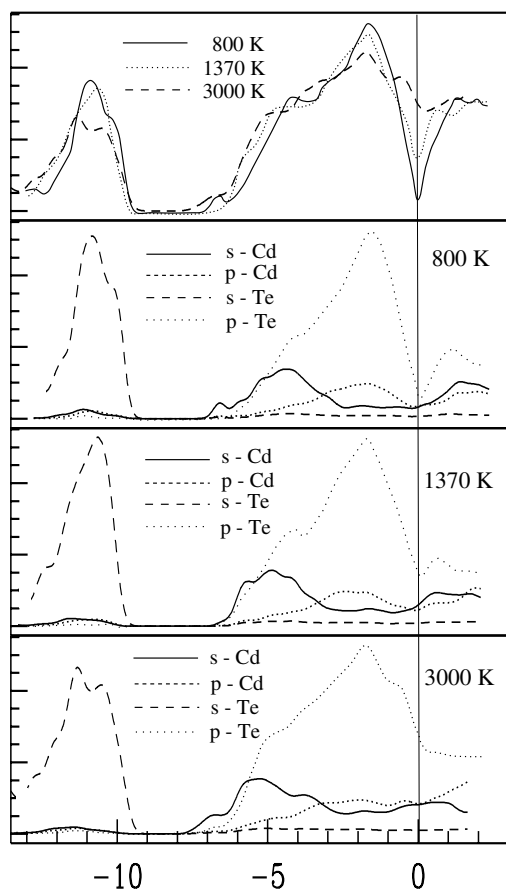


**Figure 23.** Density-of-states functions. The upper panel represents the total density of states of all valence electrons. The lower three panels represent partial densities of states at 800 K, 1370 K and 3000 K (only s and p projections of Cd and Te angular components are shown).

that is ‘washed out’ in the averaging process. Also, even if the Fermi level resides between states whose energy separation is small, the dipole matrix elements connecting these states can vanish. This is often the case, as the filled and empty states can be localized in different parts of the supercell. As a result, the conductivity has a finite gap for small  $\omega$ .

As the temperature increases, the band gap in the melt is characterized by a ‘dip’ in the DOS at the Fermi level. This dip disappears with increasing temperature. The major contribution to the states that fill the gap comes from p-like orbitals localized on the Te atoms. At 3000 K, there is a higher concentration of Te–Te bonds and consequently Te clusters with higher coordination numbers. This is reflected in the splitting of the density-of-states contributions corresponding to Te s states into  $\sigma$ -bonding and antibonding contributions. At higher temperatures, as the number of Te–Te bonds grows, the Te part of the DOS corresponding to p-like orbitals starts to resemble the valence DOS of *elemental liquid Te* [55]. As in *l*-Te, the Te p-orbital contributions in *l*-CdTe consist of  $\sigma$ -states and lone-pair (LP) states. As the number of Te–Te bonds increases in *l*-CdTe, the LP contributions are affected by disorder. Various interactions with neighbouring LP orbitals broaden the contributions to the DOS [55]. In superheated CdTe, the LP part of the DOS acquires a shoulder at  $-1$  eV. In twofold-coordinated Te, the Fermi level

is positioned between the LP and antibonding  $\sigma^*$ -states [55]. As a number of Te triplets and more complex clusters appear in the liquid, the LP contributions to the density of states become more complete and the Fermi level moves in the antibonding  $\sigma^*$ -contribution to the density of states, suggesting a semiconductor-to-metal transition. It has also been proposed [55] that in  $\ell$ -Te it is the structure transformation from a pure chain-like configuration to the configuration with a limited number of Te triplets that induces the semiconductor  $\rightarrow$  metal transition.

It is interesting to note that the peak of the conductivity occurs near  $\hbar\omega = 4$  eV independently of the melt temperature. This is close to the ‘average band gap’ in crystalline CdTe and probably represents a residual local order in the melt at the superheated temperature.

To quantify the temperature changes in the partial DOS functions, we integrate each curve representing a particular projected state up to the Fermi level (table 4). Typically, one can chose to normalize the integrals to represent the number of electrons in the supercell having a particular angular character. There is no striking evidence in this projection for ‘electron delocalization’ with increasing temperature. Specifically, one might expect delocalization of the orbitals that would result in an increase of the d- and f-state projections as a consequence of more ‘free’-electron-like or metallic-like states. However, in our system, the total number of d and f electrons on either Cd and Te sites changes by less than 0.7 electrons as the systems goes from the amorphous to the superheated state. These d and f states are not localized in the band gap.

**Table 4.** Sums of the numbers of states of different angular projections (see the text).

	800 K	1370 K	3000 K
s-Te	58.7	59.3	60.8
p-Te	103.2	102.6	100.6
d-Te	4.2	4.5	5.8
f-Te	0.1	0.2	0.4
s-Cd	29.1	29.7	30.8
p-Cd	21.9	20.6	20.0
d-Cd	6.6	6.0	5.2
f-Cd	0.8	0.8	0.7

The primary change of the orbital character in the melt is the redistribution of s and p electrons as the temperature grows. The number of s electrons increases on both Cd and Te sites, while the number of p electrons decreases. This change has been attributed to the relaxation of sp-hybridized electrons as the number of like-atom bonds increases with the temperature. Overall, one would characterize the semiconductor  $\rightarrow$  metal transition as being caused by a change of the electronic states at the Fermi level, while the rest of the states are not altered dramatically.

The diffusion constants for Cd and Te diffusing in the melt can be calculated as for the other semiconductor liquids. The results for the diffusion coefficients for the liquid near the melting point temperature and well above it are given in the table 5

**Table 5.** Diffusion constants for Cd and Te atoms in  $\ell$ -CdTe and sh-CdTe.

	$D_{\text{Cd}} (10^{-5} \text{ cm}^2 \text{ s}^{-1})$	$D_{\text{Te}} (10^{-5} \text{ cm}^2 \text{ s}^{-1})$
1370 K (theory)	6.7	5.2
1370 K (experiment [59])		5.0
3000 K (theory)	8.6	6.7

## 8. IV–VI semiconductor liquids: germanium telluride

The behaviour of GeTe appears unique in many respects. For example, crystalline GeTe undergoes an interesting phase transition. At temperatures above 700 K, GeTe exists as a B1 phase (rock-salt structure) with a coordination number of six. At temperatures below 700 K, it transforms to an A7 phase (rhombohedral structure) that consists of a stack of corrugated planes of alternating threefold-coordinated atoms. A similar transition is also observed in crystalline GeSe. This transition is believed to be the result of a *Peierls distortion*: the half-filling of the valence p band favours the alternation of short and long bonds in three almost orthogonal directions of space by opening a gap at the Fermi level. The nature of the chemical bond in both phases of GeTe has been described extensively in reference [70] and has been attributed mainly to  $pp\sigma$  resonances. That work found the degree of covalent character of the Ge–Te bonds to be larger in the *low*-temperature phase, i.e., the Peierls distorted phase. The concept of a Peierls distortion, established within the context of low-dimensional, periodic structures, has been recently generalized for aperiodic systems using a direct-space method [71].

The liquid phase of GeTe is *semiconducting* near the melting temperature ( $T_m = 1000$  K). The d.c. conductivity,  $\sigma_0$ , varies little upon melting (from 2400 to 2600  $\Omega^{-1} \text{ cm}^{-1}$ ), and increases rapidly with temperature in the liquid phase [1]. Eventually, the liquid gradually evolves to a metallic state well above the melting point. At 1170 K, a temperature at which the system may still be considered to be semiconducting, the average coordination number, deduced from neutron diffraction data [72], is equal to  $5.1 \pm 0.5$ . This value appears to be significantly smaller than that in the crystalline phase just below  $T_m$ , i.e., the rock-salt structure. The lower coordination number in the liquid was initially attributed to the appearance of numerous coordination defects, specifically vacancies, within the melt. This would also explain the increase in atomic volume observed upon melting (+6.7%). However, additional measurements near the melting point (1010 K) find a coordination number of  $3.9 \pm 0.5$  [73]. This finding makes the ‘vacancy’ hypothesis for the volume change less plausible. An alternate explanation is that the local ordering in the liquid is significantly different from that of the crystalline form. This explanation was recently suggested for GeSe, which exhibits features similar to those of GeTe in both the solid and the liquid phases [74, 75]. A change of the coordination number upon melting, combined with the persistence of a semiconducting behaviour, is unusual. One might have expected from the Joffe and Regel rule that a change in chemical ordering would result in a *metallic* not a *semiconducting* liquid.

The behaviour of liquid GeTe has been examined using first-principles molecular dynamics simulations within the PDFM as outlined for the other liquids considered here. The goal of these studies is to assess features such as microstructural changes upon melting and the electronic nature of the melt.

The partial structure factors calculated from the Fourier transforms of the partial pair correlation functions obtained by the PDFM simulations were combined using the bound coherent scattering wavelengths of hot-neutron diffraction experiments [72] to obtain the total structure factor of figure 24. The overall agreement with the experiment is quite good, especially for the right shoulder of the first peak around  $3 \text{ \AA}^{-1}$ . The partial pair correlation functions are given in figure 25. Defining the first coordination shell in terms of the location of the first minimum of the total  $g(r)$ , one can estimate the total and partial coordination numbers,  $Z$ . The major contribution to the total  $g(r)$  is from Ge–Te bonds ( $Z(\text{Ge–Te}) = 2.87 \pm 0.09$ ). However, a relatively high proportion of homopolar Ge–Ge bonds exist in the liquid ( $Z(\text{Ge–Ge}) = 2.56 \pm 0.09$ ), in addition to Te–Te bonds ( $Z(\text{Te–Te}) = 1.11 \pm 0.09$ ). The total coordination of Ge atoms ( $Z(\text{Ge})$ ) is equal to  $5.43 \pm 0.19$ , whereas for Te atoms,  $Z(\text{Te})$  is equal to  $3.98 \pm 0.18$ . These values appear to exclude the possibility of tetrahedrally bonded



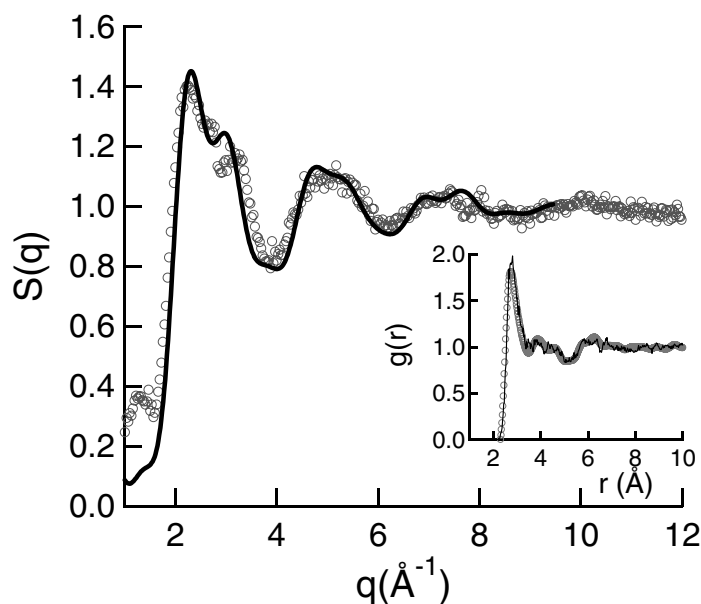


**Figure 24.** The calculated GeTe structure factor  $S(q)$  at 1000 K (solid line) compared to the neutron diffraction results [72]. Inset: the pair correlation function,  $g(r)$ .

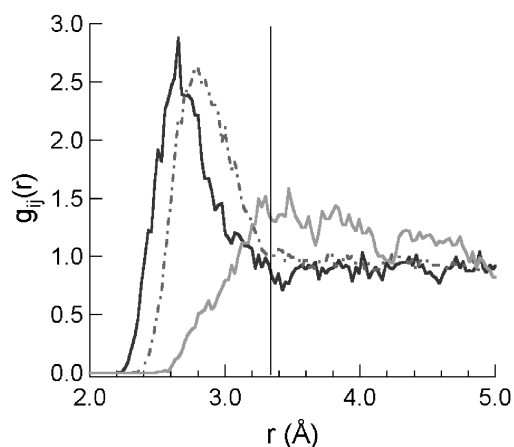


**Figure 25.** GeTe partial pair correlation functions  $g_{ij}(r)$  calculated by simulation at 1000 K:  $g_{\text{GeGe}}$  (dark curve),  $g_{\text{GeTe}}$  (dash-dot curve),  $g_{\text{TeTe}}$  (grey curve). The vertical line indicates the first minimum of the total  $g(r)$ .

Ge as suggested recently in [76] for amorphous GeTe. Also, the local order within the liquid seems to differ widely from both the low-temperature and the high-temperature crystalline forms. However, one notes that the heteropolar coordination number is very close to the value of 3 found in the Peierls distorted structure of the low-temperature crystal. This suggests that the semiconducting liquid structure (just above the melting temperature) could be closely related to the crystalline low-temperature phase. At higher temperatures, as the system evolves to a metallic state, the associated local ordering may gradually disappear in favour of homopolar

Ge–Ge bonds. Two questions must be addressed to confirm this hypothesis: (i) what is the degree of chemical ordering in the liquid; and (ii) does the molten phase exhibit a Peierls distortion?

To quantify the ordering, one can use the Warren–Cowley parameter as generalized for liquids by Wagner and Ruppertsberg [77]:

$$\alpha_x = \frac{1 - Z_{\text{Te-Ge}}/[c_{\text{Ge}}c_{\text{Te}}(Z_{\text{Ge}} + Z_{\text{Te}})]}{1 - Z_x/[c_{\text{Ge}}c_{\text{Te}}(Z_{\text{Ge}} + Z_{\text{Te}})]} \quad (23)$$

where  $c_{\text{Ge}} = c_{\text{Te}} = 0.5$  are the concentrations in Te and Ge, and the subscript  $x = \{\text{Ge}, \text{Te}\}$ . A value of  $\alpha_x = 1$  corresponds to a complete chemical ordering (alternating species),  $\alpha_x = 0$  is obtained for a random mixing of the atoms and  $\alpha_x = -1$  would be for complete phase separation. We obtain  $\alpha_{\text{Ge}} = 0.17 \pm 0.02$  and  $\alpha_{\text{Te}} = 0.32 \pm 0.05$  at 1000 K. One can interpret this configuration as the liquid being partly ordered, especially around Te atoms.

As evidence that this partial order is similar to the Peierls distortion of the crystal, one can examine an angle-constrained bond–bond correlation function,  $P(|\vec{R}_1|, |\vec{R}_2|)$  [78, 79]. This function is defined as the probability of finding an atom whose nearest neighbours are at a distance  $\{|\vec{R}_1|, |\vec{R}_2|\}$  from a given atom. In addition, a constraint is placed on the angle,  $\theta_{1,2}$ , between  $\vec{R}_1$  and  $\vec{R}_2$  (where  $\theta_{1,2} = \cos^{-1}(\vec{R}_1 \cdot \vec{R}_2/|\vec{R}_1||\vec{R}_2|)$ ). One demands  $180 - \theta_{1,2} < \theta_0$ , so that the two vectors  $\{\vec{R}_1, \vec{R}_2\}$  are almost in a ‘straight line’; see figure 26. Typically,  $\theta_0$  is taken to be  $\sim 15^\circ$ .

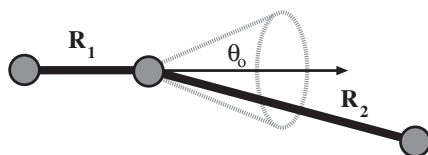
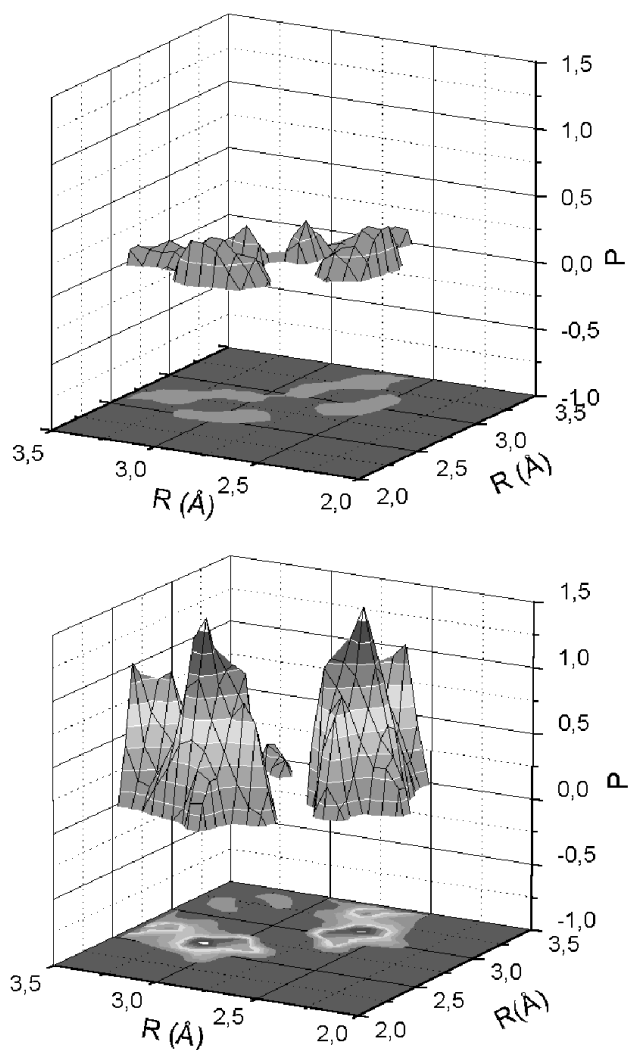


Figure 26. Definitions of  $\vec{R}_1$ ,  $\vec{R}_2$  and  $\theta_0$ .

At high temperatures (e.g. the initial configuration thermalized at a fictive temperature of 6000 K), there is no correlation between the lengths of two successive bonds; i.e., fixing  $|\vec{R}_1|$  has no effect on  $|\vec{R}_2|$ . In contrast, at the final temperature of 1000 K, a strong correlation appears, the likeliest situation being that a ‘short’ first distance is associated with a longer distance within the angular aperture of the cone (figure 26). This is the *fingerprint* of the Peierls distortion of the low-temperature crystal phase of GeTe. Further inspection of the ‘almost aligned’ triplet partial correlation functions shows the correlation is negligible for non-alternating triplets (e.g., Ge–Ge–Te), whereas it gets very large for alternating triples (Ge–Te–Ge or Te–Ge–Te). This is illustrated in figure 27. The correlation maximum is located at  $(|\vec{R}_1|, |\vec{R}_2|) = (2.7 \text{ \AA}, 3.1 \text{ \AA})$ , values very similar to the first- and the second-neighbour distances within the low-temperature crystal phase (2.84 \AA and 3.15 \AA, respectively).

As for the other liquids discussed, it is possible to quantify the atomic dynamics within the melt through the diffusion constants. In figure 28, we illustrate the squared atomic displacement as a function of time. These constants were determined by considering a 0.5 ps window over a 2 ps simulation. The diffusion constants obtained were  $D_{\text{Ge}} \approx 4.6 \times 10^{-5} \text{ cm}^2 \text{ s}^{-1}$  and  $D_{\text{Te}} \approx 1.1 \times 10^{-5} \text{ cm}^2 \text{ s}^{-1}$ . The appreciable difference (by almost a factor of four) between the diffusion constants of Ge and Te cannot be accounted for simply by the mass differences. The fact that Ge has a higher mobility instead expresses the fact that a fraction of the Ge atoms move freely in the liquid, while the remaining Ge atoms bond with Te and move as larger molecules. The Te atoms can be imagined as fixed to their local environment and ‘dragging’ it with them, which reduces their mobility.



**Figure 27.** Comparison of the constrained bond-bond correlation functions for non-alternating A-A-A triplets (upper figure) and alternating A-B-A triplets (lower figure) at 1000 K.

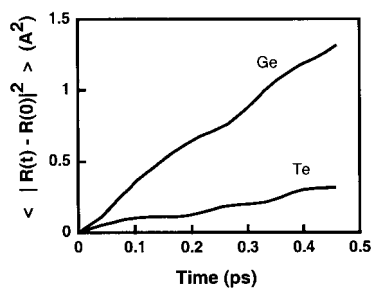


**Figure 28.** The time dependence of the mean square displacement of atoms in liquid GeTe. The simulation temperature is 1000 K.

Experimentally, the d.c. electrical conductivity of liquid GeTe at the melting temperature is similar to the conductivity of the crystal at that temperature. ( $\sigma_0 = 2600 \Omega^{-1} \text{ cm}^{-1}$  for the melt and  $2400 \Omega^{-1} \text{ cm}^{-1}$  for the crystal.) As the temperature increases the d.c. conductivity of the melt increases, reflecting the semiconducting character of the liquid [72]. We can estimate this conductivity as for GaAs and CdTe. The conductivity calculated from equation (20) is illustrated in figure 29. One can extrapolate the frequency-dependent conductivity to zero frequency to estimate the d.c. conductivity. Such an extrapolation of  $\sigma(\omega)$  to  $\omega = 0$  gives a value of the d.c. conductivity of  $\sim 3000 \Omega^{-1} \text{ cm}^{-1}$ . Given the usual caveats of such an extrapolation and the errors inherent within the formalism such as the ‘band-gap’ problem and calibrating the experimental and theoretical temperatures, the agreement is quite good. We also note that  $\sigma(\omega)$  increases with  $\omega$  to reach a maximum between 1.5 and 3 eV (figure 29). This is the signature of a semiconducting liquid, as  $\sigma(\omega)$  would decrease from  $\omega = 0$  in the case of a metal.

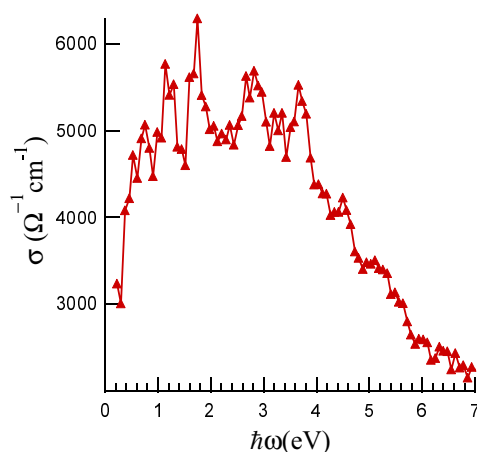


**Figure 29.** The real part of the optical conductivity for liquid GeTe at 1000 K.

## 9. Summary

We have illustrated in this review how one can simulate the properties of semiconductor liquids. In particular, we illustrated how the pseudopotential–density functional method (PDFM) can be used to perform simulations of a variety of semiconductor liquids. The introduction of the PDFM has dramatically altered the field of molecular dynamics by providing a means of extracting ‘quantum forces’. These forces can be used in *ab initio* simulations of the liquid state. In contrast to classical simulations, which use empirical interatomic forces, quantum forces eliminate any *ad hoc* assumptions about the interatomic forces. For example, charge transfer, coordination changes and rehybridization are accurately reproduced within the PDFM. This eliminates any ambiguity arising from the transcription of classical interactions to quantum ones. In addition, the *electronic* states of the melt are known at each time step of the simulation. This allows one to examine optical and dielectric properties of the melt.

In general, simulations have played a prominent role in the study of liquids. Unlike solid-state phases where the structures are fixed, and known for crystalline matter, liquids involve complex, dynamical interactions where the nature of the chemical bond is continually changing. Such systems do not lend themselves to an analysis of physical properties based

on averages over spatial coordinates. For liquids, one must examine temporal phenomena and average over time and space to understand properties. We have provided some illustrations here of how this process might be carried out for semiconductor liquids. However, one should note that this field is still in its infancy. A number of liquids have not been examined and, unlike the situation for semiconductor solids, there are no guiding empirical rules [65] that one can use for band-gap engineering. Liquid simulations should help to provide insights and invaluable guidance as we pursue a deeper understanding of this state of matter.

## Acknowledgments

We would like to acknowledge support from the National Science Foundation, NASA and the Minnesota Supercomputing Institute.

## References

- [1] Glazov V M and Shchelikov O D 1984 *Sov. Phys.–Semicond.* **18** 411  
Glazov V M, Chizhevskaya S N and Glagoleva N N 1969 *Liquid Semiconductors* (New York: Plenum)
- [2] Stich I, Car R and Parrinello M 1991 *Phys. Rev. B* **44** 4262  
Stich I, Car R and Parrinello M 1989 *Phys. Rev. Lett.* **63** 2240  
Zhang Q-M, Chiarotti G, Selloni A, Car R and Parrinello M 1990 *Phys. Rev. B* **42** 5071  
Kulkarni R V and Stroud D 2000 *Phys. Rev. B* **62** 4991  
Kulkarni R V and Stroud D 1997 *Phys. Rev. B* **55** 6896
- [3] Ciccotti G, Frenkel D and McDonald I R (ed) 1987 *Simulation of Liquids and Solids* (Amsterdam: North-Holland)
- [4] Broughton J Q and Li X P 1987 *Phys. Rev. B* **35** 9120  
Stillinger F H and Weber T A 1985 *Phys. Rev. B* **31** 5262  
Kluge M D, Ray J D and Rahman A 1987 *Phys. Rev. B* **36** 4234  
Leudtke D and Landman U 1989 *Phys. Rev. B* **40** 1164
- [5] Car R and Parrinello 1985 *Phys. Rev. Lett.* **55** 2471  
Car R and Parrinello 1988 *Phys. Rev. Lett.* **60** 204  
A recent review of the Car–Parrinello and related methods can be found in  
Marx D and Hutter J 2000 *Ab initio* molecular dynamics: theory and implementation *Modern Methods and Algorithms of Quantum Chemistry* ed J Grotenдорst (Jülich: John von Neumann Institute for Computing, Forschungszentrum) pp 301–449
- [6] Kohn W and Sham L 1965 *Phys. Rev.* **140** A1133  
Hohenberg P and Kohn W 1964 *Phys. Rev.* **136** B864  
Lundqvist S and March N H 1983 *Theory of the Inhomogeneous Electron Gas* (New York: Plenum)  
Perdew J P, Burke K and Wang Y 1996 *Phys. Rev. B* **54** 16 533  
Parr R G and Yang W 1989 *Density Functional Theory of Atoms and Molecules* (New York: Oxford)
- [7] Fermi E 1934 *Nuovo Cimento* **11** 157
- [8] Hamann D R, Schlüter M and Chiang C 1979 *Phys. Rev. Lett.* **43** 1494  
Kerker G 1980 *J. Phys. C: Solid State Phys.* **13** L189  
Vanderbilt D 1985 *Phys. Rev. B* **32** 8412  
Rappe A, Rabe K M, Kaxiras E and Joannopoulos J D 1990 *Phys. Rev. B* **43** 1227  
Cohen M L and Chelikowsky J R 1988 *Electronic Structure and Optical Properties of Semiconductors* (*Springer Series in Solid State Science* vol 75) (Berlin: Springer)
- [9] Chelikowsky J R and Cohen M L 1992 *Ab initio* pseudopotentials for semiconductors *Handbook on Semiconductors* vol 1, ed P Landsberg (Amsterdam: Elsevier) p 59  
Chelikowsky J R and Louie S G (ed) 1996 *Quantum Theory of Real Materials* (Dordrecht: Kluwer)  
Pickett W E 1989 *Comput. Phys. Rep.* **9** 115  
Chelikowsky J R 2000 *J. Phys. D: Appl. Phys.* **33** R33
- [10] Cohen M L, Schlüter M, Chelikowsky J R and Louie S G 1975 *Phys. Rev. B* **12** 5575 and references therein
- [11] Godlevsky V and Chelikowsky J R 1998 *J. Chem. Phys.* **109** 7312
- [12] Phillpot S R, Yip S and Wolf D 1989 *Comput. Phys.* **3** 20
- [13] Sugino O and Car R 1995 *Phys. Rev. Lett.* **74** 1823

- [14] Nosé S 1984 *Mol. Phys.* **52** 255  
Nosé S 1984 *J. Chem. Phys.* **81** 511
- [15] Kubo R 1966 *Rep. Prog. Theor. Phys.* **29** 255  
Risken H 1984 *The Fokker–Planck Equation* (Berlin: Springer)  
Stratonovitch R L 1963 *Topics in the Theory of Random Noise* (New York: Gordon and Breach)  
van Kampen N G 1981 *Stochastic Processes in Physics and Chemistry* (Amsterdam: North-Holland)
- [16] Examples of Langevin applications include those given by  
Tully J C, Gilmer G and Shugart M 1979 *J. Chem. Phys.* **71** 1630  
Biswas R and Hamann D R 1986 *Phys. Rev. B* **34** 895  
Binggeli N and Chelikowsky J R 1994 *Phys. Rev. B* **50** 11764
- [17] Binggeli N, Martins J L and Chelikowsky J R 1992 *Phys. Rev. Lett.* **68** 2956
- [18] Verlet L 1967 *Phys. Rev.* **165** 201  
Beeman D 1976 *J. Comput. Phys.* **20** 130
- [19] Wentzcovitch R M and Martins J L 1991 *Solid State Commun.* **78** 831  
Binggeli N, Martins J L and Chelikowsky J R 1992 *Phys. Rev. Lett.* **68** 2956  
Chelikowsky J R and Binggeli N 1993 *Solid State Commun.* **88** 381  
Chelikowsky J R and Binggeli N 1994 *Phys. Rev. B* **49** 114
- [20] Troullier N and Martins J L 1991 *Phys. Rev. B* **43** 1993
- [21] Kleinman L and Bylander D M 1982 *Phys. Rev. Lett.* **48** 1425
- [22] Ihm J, Zunger A and Cohen M L 1979 *J. Phys. C: Solid State Phys.* **12** 4409
- [23] Saad Y, Stathopoulos A, Chelikowsky J R, Wu K and Ögüt S 1996 *BIT* **36** 563  
Stathopoulos A, Ögüt S, Saad Y, Chelikowsky J R and Kim H 2000 *Comput. Sci. Eng.* **2** 19  
Louie S G 1985 *Electronic Structure, Dynamics and Quantum Structural Properties of Condensed Matter* (New York: Plenum) p 335
- [24] Chan C T, Bohnen K P and Ho K M 1993 *Phys. Rev. B* **47** 4771
- [25] Emsley J 1996 *The Elements* 3rd edn (Oxford: Oxford University Press)
- [26] Virkkunen R, Laasonen K and Nieminen R 1991 *J. Phys.: Condens. Matter* **3** 7455
- [27] Ziman J 1979 *Models of Disorder* (Cambridge: Cambridge University Press)
- [28] Kubo R 1957 *J. Phys. Soc. Japan* **12** 570  
Greenwood D 1958 *Proc. Phys. Soc.* **71** 585
- [29] Hybertsen M S and Louie S G 1986 *Phys. Rev. B* **34** 5390
- [30] Godlevsky V, Chelikowsky J R and Troullier N 1995 *Phys. Rev. B* **52** 13 281
- [31] Waseda Y 1980 *The Structure of Non-Crystalline Materials* (New York: McGraw-Hill)
- [32] Jank W and Hafner J 1990 *Phys. Rev. B* **41** 1497
- [33] Kresse G and Hafner J 1994 *Phys. Rev. B* **49** 14 251
- [34] Stich I, Car R and Parrinello M 1991 *Phys. Rev. B* **44** 4262
- [35] Bergman C, Bichara C, Chieux P and Gaspard J 1985 *J. Physique. Coll.* **46** C8 97
- [36] Hafner J and Jank W 1989 *J. Phys.: Condens. Matter* **1** 4325
- [37] Zhang Q-M, Chiarotti G, Selloni A, Car R and Parrinello M 1990 *Phys. Rev. B* **42** 5071
- [38] Molteni C, Colombo L and Miglio L 1994 *J. Phys.: Condens. Matter* **6** 5255
- [39] Faken D and Jonsson H 1994 *Comput. Mater. Sci.* **2** 279
- [40] Honeycutt J and Andersen H 1987 *J. Phys. Chem.* **91** 4950
- [41] Jonsson H and Andersen H 1988 *Phys. Rev. Lett.* **60** 2295
- [42] Van Vechten J A 1972 *Phys. Rev. Lett.* **29** 769
- [43] Van Vechten J A 1973 *Phys. Rev. B* **7** 1479
- [44] Arthur J 1967 *J. Phys. Chem. Solids* **28** 2257
- [45] Ilegems M and Pearson J 1975 *Annu. Rev. Mater. Sci.* **5** 345
- [46] Li X-P, Allen P, Car R, Parrinello M and Broughton J 1989 *Phys. Rev. B* **41** 3260
- [47] Holender J, Payne M and Simpson A 1995 *Phys. Rev. B* **52** 967
- [48] Hellwege K (ed) 1984 *Landolt–Bornstein New Series* (Berlin: Springer)
- [49] Zanio K 1978 *Semicond. Semimet.* **13**
- [50] Rudolph P and Muhlberg M 1993 *Mater. Sci. Eng. B* **16** 8
- [51] Larson D J 1994 *Micrograv. News* **1** 10
- [52] Godlevsky V, Derby J and Chelikowsky J R 1998 *Phys. Rev. Lett.* **81** 4959
- [53] Gaspard J, Bergman C, Bichara C, Bellissent R, Chieux P and Coffard J 1987 *J. Non-Cryst. Solids* **97+98** 1283
- [54] Glazov V and Pavlova L 1998 *J. Cryst. Growth* **184+185** 1253
- [55] Gaspard J, Raty J, Ceolin R and Bellissent R 1996 *J. Non-Cryst. Solids* **205–207** 75
- [56] Joffe A and Regel A 1960 *Progress in Semiconductors* vol 4 (London: Heywood) p 237

- [57] Lee I and Chang K 1994 *Phys. Rev. B* **50** 18 083
- [58] Kröger P 1973 *The Chemistry of Imperfect Crystals* vol 1 (New York: Elsevier) p 195
- [59] Rudolph P 1994 *Prog. Cryst. Growth Charact.* **29** 275
- [60] Jordan M 1970 *Metall. Trans.* **1** 239
- [61] Lichter B and Sommelet P 1969 *Trans. AIME* **245** 1021
- [62] Louie S, Froyen S and Cohen M 1982 *Phys. Rev. B* **26** 1738
- [63] McShimin H and Thomas D 1962 *J. Appl. Phys.* **33** 56
- [64] Berlincourt D, Jaffe H and Shiozawa L 1963 *Phys. Rev.* **129** 1009
- [65] Phillips J C 1973 *Bands and Bonds in Semiconductors* (New York: Academic)
- [66] Yao M and Endo H 1996 *J. Non-Cryst. Solids* **205–207** 85
- [67] Bichara C, Raty J and Gaspard J 1996 *J. Non-Cryst. Solids* **205–207** 361
- [68] Shcherbak L 1998 *J. Cryst. Growth* **184+185** 1057
- [69] Hybertsen M and Louie S 1988 *Phys. Rev. B* **38** 4033
- [70] Polatoglou H M, Theodorou G and Economou N A 1983 *J. Phys. C: Solid State Phys.* **16** 817
- [71] Gaspard J-P, Pellegatti A, Marinelli F and Bichara C 1998 *Phil. Mag.* **B 77** 727 and references therein
- [72] Raty J-Y, Gaspard J-P, Bionducci M, Céolin R and Bellissent R 1999 *J. Non-Cryst. Solids* **250–252** 277
- [73] Raty J-Y 1990 *PhD Thesis* University of Liège
- [74] Salmon P S and Liu J 1994 *J. Phys.: Condens. Matter* **6** 1449
- [75] Petri I, Salmon P S and Fisher H E 1999 *J. Phys.: Condens. Matter* **11** 7051
- [76] Hosokawa S, Hari Y, Kouchi T, Ohno I, Taniguchi M, Hiraya A, Takata Y, Kosugi N and Watanabe M 1998 *J. Phys.: Condens. Matter* **10** 1931
- [77] Wagner C and Ruppertsberg H 1981 *At. Energy Rev.* **1** 101
- [78] Bichara C, Pellegatti A and Gaspard J-P 1993 *Phys. Rev. B* **47** 5002
- [79] Raty J Y, Godlevsky V, Ghosez Ph, Bichara C, Gaspard J P and Chelikowsky J R 2000 *Phys. Rev. Lett.* **85** 1950